

COLD-ELECTRON BOLOMETERS

WITH THIN ABSORBERS AND IMPROVED SIN AND SIS'
JUNCTIONS FOR THE BOOMERANG BALLOON PROJECT

HANNES KUUSISTO
ANNA KARLSSON
OSKAR LINDGREN
ANTON FRISK KOCKUM
DANIEL MIDTVEDT

Department of Microtechnology and Nanoscience
CHALMERS UNIVERSITY OF TECHNOLOGY
Göteborg, Sweden
Bachelor Thesis 2009

Cold-Electron Bolometers

with Thin Absorbers and improved SIN and SIS' Junctions for the BOOMERanG
Balloon Project

HANNES KUUSISTO

ANNA KARLSSON

OSKAR LINDGREN

ANTON FRISK KOCKUM

DANIEL MIDTVEDT

© HANNES KUUSISTO, ANNA KARLSSON, OSKAR LINDGREN,
ANTON FRISK KOCKUM AND DANIEL MIDTVEDT, 2009.

Department of Microtechnology and Nanoscience

Chalmers University of Technology

SE-412 96 Göteborg

Sweden

Telephone + 46 (0)31-772 3608

Cover:

The CAD layout for sample L8-21 which has the BOOMerang structure, a close-up of the part of the CAD where the absorber and the junctions of a Cold-Electron Bolometer is connected with its antenna, another close-up taken with an optical microscope and an AFM picture of a similar junction.

Chalmers reproservice

Göteborg, Sweden 2010

Abstract

This thesis concerns the fabrication of Cold-Electron Bolometers (CEBs) with shadow angle evaporation technique, suitable for measuring the Cosmic Microwave Background Radiation as a part of the BOOMERanG project. We have studied two possible improvements of the absorber.

Firstly, we have decreased the thickness of the aluminium layer at the top of the absorber (7, 10, 15, 20 nm) in order to see if a smaller absorber volume would improve the bolometer. We have seen that bolometers with arrays of Superconductor-Insulator-Normal Metal (SIN) junctions exhibit improved characteristics for thinner absorbers. Estimates show that with these changes, the CEBs can soon meet with the noise requirements for the BOOMERanG project. We have also confirmed that larger arrays are saturated at a higher powerload, as it is distributed among the absorbers.

Secondly, we varied the thickness of the chromium layer at the bottom of the absorber (0.1, 0.2, 0.3, 0.5 nm) to see if we could achieve a bolometer with Superconductor-Insulator-Weak Superconductor (SIS') junctions. We found that the thinnest chromium layer did not fully suppress the superconducting properties of aluminium, but with the current equipment of the Bolometer Group at Chalmers it is probably impossible to repeatedly reproduce a weak superconductor with a specific critical temperature using this method.

Keywords: Cold-Electron Bolometer (CEB), shadow angle evaporation, absorber, SIN junction, SIS junction, BOOMERanG.

Sammanfattning

Denna rapport behandlar tillverkningen av kallelektron-bolometrar (CEB) med skuggevaporeringssteknik, lämpliga för mätning av den kosmiska bakgrundsstrålningen som en del av BOOMERanG-projektet. Vi har undersökt två möjliga förbättringar av absorbatoren, som är en av de viktigaste delarna i en CEB.

Vi har dels, för att undersöka om en minskning av absorbatorvolymen förbättrar bolometern, ändrat tjockleken (7, 10, 15, 20 nm) på det aluminiumlager som utgör överdelen av absorbatoren. Vi har sett att bolometrar med seriekopplade Supraledare-Isolator-Normalmetall-övergångar (SIN-övergångar) uppvisar förbättrad karakteristik för tunnare absorbatörer. Uppskattningar visar att med dessa ändringar kan BOOMERanG-projektets krav på känslighet snart uppfyllas med de parametrar vi använt. Vi har också bekräftat att fler bolometrar kopplade i serie mätts vid en högre belastning, vilken fördelas mellan de enskilda bolometerna.

Vi har också, för att se om vi kan tillverka en bolometer med Supraledare-Isolator-Svag Supraledare-övergångar (SIS'-övergångar), varierat tjockleken (0.1, 0.2, 0.3, 0.5 nm) hos det kromlager som ligger underst i absorbatoren. Vi fann att det tunnaste kromlagret inte undertryckte aluminiums supraledande egenskaper fullständigt, men med de begränsningar som finns hos utrustningen hos Bolometergruppen på Chalmers är det antagligen omöjligt att upprepade gånger framställa en svag supraledare med en specifik kritisk temperatur med denna metod.

Nyckelord: kallelektron-bolometer (CEB), skuggevaporering, absorbator, SIN-övergång, SIS-övergång, BOOMERanG.

Preface & Acknowledgements

The journey we bachelor students have undertaken as part of the Bolometer Group at Chalmers this year of 2009 has been wonderful. When choosing among the different subjects for bachelor theses at Chalmers, we set out to find a project which would provide us with ample theoretical and experimental challenges and give us the opportunity to work close to the front lines of an interesting scientific field. Once we found the Cold-Electron Bolometer project, the choice was easy. Looking back six months later, we can only say that our expectations were fulfilled. During this spring we have had the opportunity to greatly expand our knowledge in the fields of superconductivity, nano device fabrication and in the theory of the Cosmic Background Radiation. One of the best weeks during this time we spent at the Björkliden Workshop on Cryogenic Detectors, where we not only met many brilliant and generous minds, but also tried to make it into the Guinness Book of World Records by making the world's strongest igloo.

The past few months we have been alternately exhilarated, puzzled, hopeful, pessimistic, intrigued and exhausted. In the end, we somehow produced the thesis you are now holding in your hands. Before you start the interesting reading we would like to remind you that a work such as the one presented here never is done solely by the authors, not even when there are five of them.

First of all we would like thank our supervisor, Professor Leonid Kuzmin, for his support, his positive attitude, his untiring and patient answers to all our questions and for giving us the opportunity to visit the Björkliden workshop.

We are very grateful to Mikhail Tarasov for devoting so much of his time to our cleanroom and cryolab education, for his attention to details during valuable discussions and also for the vegetarian glögg.

We are also very grateful to Sumedh Mahashabde for helping us out with all parts of the fabrication process and the measurements, for his cheerfulness and for telling us that Swedish trains are nowhere near crowded. Moreover, we would like to thank Ernst Otto for his assistance in the wafer fabrication

and for his FINline expertise.

Andreas Myrin gladly introduced us to the CEB concept when we were starting our work. He, Virginia Claudio and Ankit Bisht paved the way for our work by their investigations last year. We would also like to thank Virginia and Ankit for their company in Björkliden. Thanks are also due to the Chalmers Centre for Language and Communication, whose representatives helped us bring this thesis to another level. Furthermore, this work was supported by STINT, SI, VR, SNSB and MC2.¹

Neither the last nor the least: to our families, who have supported our dreams for so long, we extend our heartfelt gratitude. Finally, thanks to all the participants of the Björkliden workshop who made the event an everlasting memory. The knowledge we gained about T-matrices and TES didn't make it into this thesis, but it was great fun.

¹The Swedish Foundation for International Cooperation in Research and Higher Education, the Swedish Institute, the Swedish Research Council, the Swedish National Space Board and the Microtechnology Centre at Chalmers.

Contents

1	Introduction	1
1.1	Bolometers	2
1.2	The purpose of this thesis	2
1.3	Method	3
1.4	Overview	4
2	Superconductivity Basics	6
2.1	The structure of solid metals	6
2.2	The properties of superconductors	7
2.3	The SIN junction	8
2.4	The SIS' junction	10
3	The Cold-Electron Bolometer Concept	14
3.1	The CEB in working mode	14
3.1.1	The cold-electron effect	14
3.1.2	Prevention of back-tunnelling	20
3.1.3	Voltage and current biasing	20
3.2	BOOMERanG requirements	21
3.3	An array of SIN junctions	21
3.4	SIS' lines of development	22
3.5	Noise equivalent power	24
3.5.1	Photon noise	25
3.5.2	Thermal (electron-phonon) noise	26
3.5.3	Noise in the junction	26
3.5.4	Amplifier noise	27
3.6	Expectations of a decrease in absorber volume	27
3.7	Layout of the CEB on chip	28
3.7.1	Antennas	30
4	The Manufacturing Process	32
4.1	Spinning of resist	32
4.2	E-beam lithography, postbaking and scribing	33
4.3	Development	33

4.4	Evaporation	33
4.5	Lift-off	35
4.6	Optical and electronic inspections	35
4.6.1	Optical microscope	36
4.6.2	SEM - Scanning electron microscope	36
5	Measurements	38
5.1	Electronic inspections and the AFM	38
5.1.1	Room temperature checks	38
5.1.2	Cryogenics equipment and IV curves at cryogenic temperatures	40
5.1.3	AFM - Atomic force microscope	40
5.2	IV characteristics	41
5.2.1	Resistance ratio: Subgap resistance & leakage	41
5.2.2	The energy gap of the superconductor	42
5.2.3	Saturation of absorbers	42
5.2.4	Responsivity	45
5.2.5	Response to radiation	46
6	Results & Discussion	47
6.1	Designing absorbers for SIN and SIS'	47
6.2	Junctions	48
6.2.1	Resistance ratio	50
6.2.2	Change of subgap resistance with temperature	52
6.2.3	Dynamic conductance	53
6.2.4	Conclusion	54
6.3	Absorbers	55
6.3.1	Saturation	55
6.3.2	Saturation curves	55
6.3.3	Potential decrease of leakage due to thinner absorbers	57
6.3.4	Conclusion	58
6.4	Entire Bolometers	59
6.4.1	Response to external radiation	59
6.4.2	Noise estimation	61
6.4.3	Conclusion	62
6.5	Main results and conclusions	62
7	Summary and Future Prospects	65
7.1	Future prospects	66
A	Recipes	71
A.1	L9	71
A.1.1	Layer 1	71
A.1.2	Layer 2	72

A.1.3	Layer 3	73
A.2	L10	73
A.2.1	Layer 1	73
A.2.2	Layer 2	74
A.2.3	Layer 3	74
A.3	L14	74
A.3.1	Layer 1	75
A.3.2	Layer 2	76
A.3.3	Layer 3	77
A.3.4	Layer 4	78
B	Layouts	79
C	Descriptions of some advanced equipment	84
C.1	AFM - Atomic force microscope	84
C.2	The Heliox cryo system	84
D	List of manufactured samples	87

List of Figures

1.1	The basic principle of the CEB	3
2.1	The Fermi-Dirac distribution.	7
2.2	The DOS of a superconductor.	8
2.3	The electron density in a superconductor at and around T_c	9
2.4	Electron tunnelling across an SIN junction.	9
2.5	$I(T)$ across an SIN junction.	11
2.6	IV characteristics for an SIN junction.	11
2.7	Electron tunnelling across an SIS' junction.	12
2.8	IV characteristics of an SIS' junction.	13
3.1	A visualization of an SIN junction in a CEB.	15
3.2	A simulation of electron temperatures in a CEB	18
3.3	A simulation of electron-phonon relaxation times in a CEB	18
3.4	The relaxation times τ_{cool} and τ_{e-ph} as a function of bias voltage	19
3.5	A visualization of an SIN junction with a normal metal trap.	20
3.6	An illustration of the loop geometry used in SIS' junctions.	23
3.7	A visualization of an SIS' junction	24
3.8	The layout of the ARR4 chip	29
3.9	A simplified picture of the ARR4 layout	29
3.10	The shape of the antenna used in the FINline structure.	30
3.11	The cross-slot antenna used in the ARRay structures.	31
4.1	A visualization of the shadow evaporation technique.	34
4.2	A schematic view of the Edwards evaporator.	35
4.3	A CEB structure photographed with an optical microscope	37
5.1	The experimental setup for room temperature measurements	39
5.2	2-, 3- and 4-point measurements.	39
5.3	The setup for measuring response to radiation.	41
5.4	Simulated dynamic resistance $R_d(V,T)$ of a junction	43
5.5	A descriptive plot of the resistance ratio of an SIN junction	43
5.6	Simulated dynamic conductance $\frac{dI}{dV}(V)$ of a junction	44
5.7	Simulated saturation of an array	45
5.8	Simulated voltage response $\frac{dV}{dT}(T)$ and the responsivity	46

6.1	SIS' behaviour in L14-23	49
6.2	Resistance ratio plotted as a function of the aluminium thickness.	50
6.3	Dynamic resistance $\frac{dV}{dT}(T)$ for samples with small/large leakage	53
6.4	Measured $\frac{dI}{dV}$, compared with the corresponding simulations .	54
6.5	IV curves for the T1 and FIN structures on the L10-34 sample	56
6.6	Normalized saturation curves of different absorbers	57
6.7	AFM picture of a junction from the L10-63 B1 structure . . .	58
6.8	Calculated $\frac{dV}{dT}(V)$ for the L10-63 B1 structure.	60
6.9	Responsivity S_V for the L10-63 B1 structure.	60
6.10	Radiation response for the structure L10-55 B1	61
6.11	Bolometer noise as a function of voltage for the L10-63 B1 structure.	63
B.1	The BOOM6 layout	80
B.2	The simplified BOOM6 layout	80
B.3	The ARR3 layout	81
B.4	The simplified ARR3 layout	81
B.5	The ARR4 layout	82
B.6	The simplified ARR4 layout	82
B.7	The FIN4 layout	83
B.8	The simplified FIN4 layout	83
C.1	The working principle of the AFM	85
C.2	The Heliox cooling system	85

List of Tables

6.1	Structure data for the L10-63 sample.	52
A.1	The evaporation parameters for the bolometer layer of L10-63ARR3.	75
D.1	A list of our manufactured samples	87
D.2	Data of our measured structures	88

Nomenclature

Abbreviations

ARR	Abbreviation for the structures with arrays of SIN junctions, in this thesis denoted by ARRay
BOOM	Abbreviation for the structures with single SIS' junctions, in this thesis denoted by BOOMerang
BOOMERanG	Balloon Observations Of Millimetric Extragalactic Radiation and Geophysics
BSE	Backscattered Electron
CEB	Cold-Electron Bolometer
CMBR	Cosmic Microwave Background Radiation
DOS	Density of States
FIN	Abbreviation for the structures with single SIS' junctions and finlike antennas, in this thesis denoted by FINline
FIRAS	Far-Infrared Absolute Spectrophotometer
I	Insulator
JFET	Junction Gate Field-Effect Transistor
MOSFET	Metal Oxide Semiconductor Field-Effect Transistor
N	Normal metal
NEP	Noise Equivalent Power
PTC	Pulse Tube Cooler
RR	Resistance Ratio
S	Superconductor

S'	Weak Superconductor
SC	Superconductor
SEM	Scanning electron microscope
SIN	Superconductor-Insulator-Normal metal
SIS'	Superconductor-Insulator-Weak Superconductor
SQUID	Superconducting Quantum Interference Device
STM	Scanning Tunnelling Microscope
TES	Transition Edge Sensor
WMAP	Wilkinson Microwave Anisotropy Probe

Symbols

β	The reabsorption coefficient of a tunnel junction, i.e. the fraction of electrons that back-tunnel
Δ_0	The energy gap in a superconductor at $T = 0$ K
Δ	The energy gap in a superconductor
γ	The Sommerfeld constant
Λ	Volume
Σ	A material constant connected to thermal conductance
τ_{cool}	The estimated relaxation time for the tunnel junction, i.e. the time between two tunnelling events
τ_{e-ph}	The estimated relaxation time of the electron-phonon system
Θ	The Heaviside step function
C_e	Heat capacity of electrons
e	The elementary charge
e_n	Voltage noise
$f(E)$	The Fermi-Dirac distribution
G_{cool}	The thermal conductance across the tunnel junction
G_{e-ph}	Heat conductance between electrons and phonons

h	Planck's constant
i_n	Current noise
k_B	The Boltzmann constant
N	The electron density
$N_s(E)$	Density of states of a superconductor
P_{cool}	The cooling effect of the tunnel junction due to the removal of hot electrons
P_{e-ph}	Energy transfer rate between electrons and phonons
R_d	The dynamic resistance
R_l	Leakage resistance
R_N	The resistance of the insulating barrier in an SIN or SIS' junction i.e. the normal resistance of the junction
R_S	Subgap Resistance
R_{abs}	The absorber resistance
T_c	The critical temperature of a superconductor
T_e	Electron temperature
T_F	The Fermi temperature
T_{ph}	Phonon temperature
V	Voltage
V	Volume

Little by little, one travels far.
- J.R.R. Tolkien

Chapter 1

Introduction

Four hundred thousand years after the Big Bang, elementary particles started to combine, forming neutrally charged atoms. At earlier times the plasma oscillations effectively cancelled any electromagnetic radiation, but now photons could pass freely. The universe became, for probably the first time, transparent to light. [1]

At this time, when the Cosmic Microwave Background Radiation (CMBR) was created, the temperature of the universe was approximately 3000 K. The accelerating expansion of the universe had caused it to cool down, an expansion which has continued; by now the temperature has decreased to about 2.7 K. The CMBR is possibly the most conclusive evidence for the Big Bang-theory [2]. As Prof. Paul Richards put it: “*The CMBR is the Rosetta Stone of cosmology*” [3]. In 1990, the Far-Infrared Absolute Spectrophotometer (FIRAS), measured the temperature of the CMBR, and found that it agrees with the theoretical predictions to at least 1 part in 100 000 [4].

However, the Big Bang theory also predicts anisotropies in the CMBR, at a level less than 1 part in 100 000. Later experiments, most notably WMAP (Wilkinson Microwave Anisotropy Probe), the results of which were named the Breakthrough of the Year in Science 2003 [5], have confirmed some of these anisotropies, but there are still some that have not been charted. For example, the CMBR is slightly polarized. The E-mode polarization arises naturally from the scattering of photons in the primordial plasma, while the B-mode polarization is less understood. It arises from interaction with primordial gravitational waves, and measuring it would give valuable information on the expansion rate of the early universe [6]. However, this polarization has an estimated amplitude of $0.1 \mu\text{K}$, and measuring it requires an entirely new generation of sensitive measuring devices. Among these the Cold Electron Bolometer (CEB) has a place as a promising candidate. [7] [8]

1.1 Bolometers

The name “bolometer” arises from the Latin words “bolo”, radiation and “meter”, to measure. A bolometer is an instrument for measuring radiation by the rise in temperature absorbed radiation induces. It was first invented by an American astronomer named Samuel Pierpont Langley [9]. Langley’s bolometer utilized the thermoelectric effect to measure the temperature, and thus indirectly the radiation. With his invention Langley was the first to measure the formerly invisible infrared part of the spectrum. Today, 131 years later, the basic premise behind Langley’s instrument is still superior to other instruments for measuring radiation in the infrared region. Several devices use this old concept, among those the Transition Edge Sensor (TES) and the Cold-Electron Bolometer (CEB). However, the modern bolometers consist of nanostructures evaporated onto chips smaller than a thumbnail, cooled down to cryogenic temperatures of a few hundred millikelvins, utilizing tunnelling currents between superconducting materials for precise measurements.

In the CEB, the radiation is led by antennas to a thin metal strip called the absorber. The absorber is either made of a normal metal (N) or a weak superconductor (S’) and is a critical part of the CEB. It is separated from two superconducting contacts by a thin insulating layer (I), forming a tunnel junction (SIN/SIS’). The incoming radiation excites electrons in the absorber, causing them to tunnel through the junctions. An applied bias voltage directs the flow of current, which can be read out and converted to a temperature reading. Depending on how large a bias voltage is applied over the junction, the device will be more or less sensitive to incoming radiation. The setup is illustrated in figure 1.1.

1.2 The purpose of this thesis

The purpose of this bachelor thesis is to examine a possible improvement of the absorber: a decrease of the absorber thickness, both for use in the existing SIN junctions and in order to create SIS’ junctions. The work has been done within the Bolometer Group at Chalmers, led by Leonid Kuzmin, where the CEB concepts are researched. It is the latest development on CEB technology, with additional variations of other parameters as a part of the search for improvements. The two bolometer concepts that have been studied are the Cold-Electron Bolometer with SIS’ and Josephson Tunnel Junctions [10] and the Array of Cold-Electron Bolometers with SIN Tunnel Junctions [11][12].

Several years ago the Bolometer Group at Chalmers radically changed the CEB fabrication methods by flipping the design upside down in order

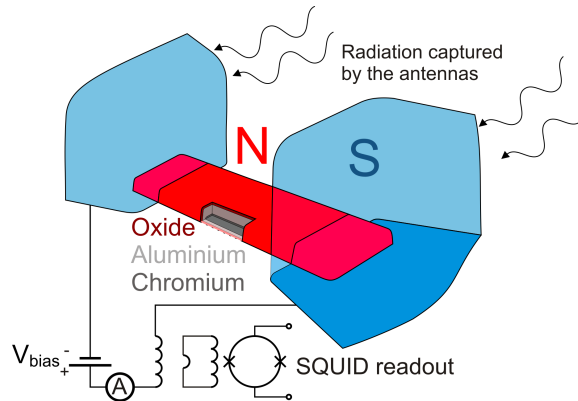


Figure 1.1: The basic design of the CEB, illustrated for an SIN junction. The incoming radiation is led through antennas via the superconducting Al contacts to the absorber made of Al and Cr. The contacts are separated from the absorber by an oxidized layer of Al, which acts as an insulator. Electrons excited in the absorber by the incoming radiation tunnel through the SIN tunnel junction to the right (due to the V_{bias}), and the current is read out using an operational amplifier or a SQUID, where the latter is the more effective choice for an SIN junction.

to be able to make junctions with thinner absorbers and improved characteristics. Recent studies have shown that a chromium layer with a thickness of 0.5 nm directly below a 20 nm layer of aluminium suppresses the critical temperature of the thin film below 50 mK [13] so that a normal metal absorber can be created. This was the lowest absorber thickness previously used. For the SIN junctions we have decreased these thicknesses even further and evaluated the impact on the performance of the bolometer. For the SIS' junctions a weakly superconducting absorber with critical temperature in the range of 100 – 300 mK was needed, and we have reduced the amount of chromium to see if this can be achieved. With no chromium layer at all, the critical temperature of the aluminium would be 1.2 K [14].

The improvements of the CEBs are done partly because the Bolometer Group has been invited by the BOOMERanG project to develop CEBs with JFET readout for measurements at 350 GHz. BOOMERanG (Balloon Observations Of Millimetric Extragalactic Radiation and Geophysics) is dedicated to measurements of the CMBR at high altitude in the Arctic and Antarctic regions. The project boasts two previous successful flights in 1998 and 2003; the next flight is planned for 2011. [15] [16]

1.3 Method

Our work with the CEBs within the Bolometer Group has been both practical and theoretical. We have grasped the basic concepts of the CEBs as well as more advanced knowledge, and put this information to use while

evaluating the CEB structures we fabricated. Thus our work ranges from literature studies to cleanroom fabrication of CEB samples and cryogenic measurements on the IV characteristics of the fabricated structures. Moreover we have analyzed the measured IV characteristics through both theoretical simulations of the significant parameters as well as interpretations of the obtained data with the help of MATLAB computer programs we wrote solely for this purpose.

1.4 Overview

This section provides an overview of the different chapters to guide the reader through the report. When a chapter contains information mainly based on a few sources, they are mentioned here instead of in the text. A lot of our knowledge has been gained through private communications with our supervisor Leonid Kuzmin and Michael Tarasov during the spring. When possible we have given references to articles in the thesis, but too much of what we have learnt from Kuzmin and Tarasov is too widespread in the text. The two references to Kuzmin and Tarasov are better placed here [17] [18].

The flow of this report is as follows:

The next chapter, **Superconductivity Basics**, is meant to introduce the reader to the theory behind the SIN and SIS' junctions. It begins with a short description of the properties of metals and continues with an overview of important concepts such as density of states, Cooper pairs and critical temperature. Finally, it ends with a section each on SIN and SIS' junctions and their IV characteristics. The information is mainly based on [19] and [20].

In chapter 3, **The Cold-Electron Bolometer Concept**, the modern CEB is described in detail: how and why it works, what BOOMERanG requires of the CEBs and what development lines we have been working with within the Bolometer Group. Issues like heat dissipation in the absorber, noise and the expectations on a decrease of the absorber volume are also introduced.

The fabrication of bolometer samples is brought to light in chapter 4, **Manufacturing Process**. Here the steps spinning of resist, e-beam lithography, development, evaporation and lift-off are explained. The equipment and the methods used to perform optical inspection on the bolometers are also described. Chapter 5, **Measurements**, continues by describing the methods for electronic characterization of the bolometer samples. The last section of **Measurements** delves into the subject of interpreting the numerous IV curves our measurements produced.

Following this, the results of our experiments are presented and discussed in detail in **Results & Discussion**. Finally, a summary of the report and

thoughts on the future prospects of the CEB development are to be found in the **Summary and Future Prospects**.

Chapter 2

Superconductivity Basics

Without a basic knowledge of superconductivity, it is difficult to understand the operational functions of a bolometer. Hence this chapter will be devoted to the basic theory behind superconductors. Key concepts such as electron energy distributions, electron-phonon interaction, properties of superconductors and SIN and SIS junction characteristics are presented. Using the theory presented here, the next chapter introduces the concept of the Cold-Electron Bolometer.

2.1 The structure of solid metals

A solid is characterized by the stationary pattern of atoms which is repeated over and over again, forming nodes in a crystal lattice. However, no structures are ever at a complete rest; the vibrations of the nodes relative to one another form movements called phonons. Naturally, phonons hold energy, and the ions in the structure can interact with passing electrons so that the phonons take energy from or give energy to the electrons. This results in a phenomenon where the displacement of positive ions due to passing electrons affects other electrons, a phenomenon which is called electron-phonon coupling.

Apart from the properties of solids, solid metals have another specific characteristic: the electrons can move freely within the material. They obey the laws of quantum mechanics and thus, being fermions, two of them cannot occupy the same quantum state. At the lowest energy state of a material, when the temperature is 0 K, this means that the energy states of the electrons will be filled up entirely to a certain level, known as the Fermi energy E_F . When the temperature of the system is increased, only the electrons close to the Fermi level are affected, and that in such a way as to make the previously sharp boundary smeared. To describe to what extent each energy level is filled with electrons, the Fermi-Dirac distribution $f(E)$ is used. This

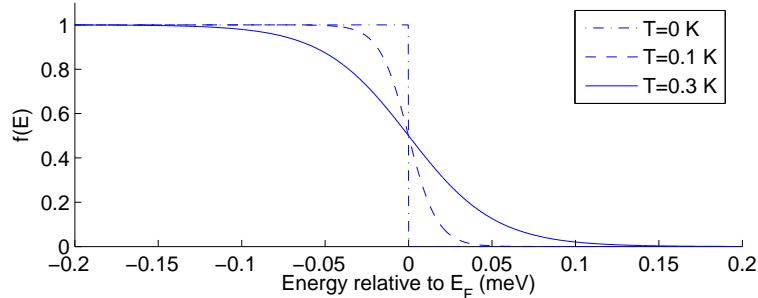


Figure 2.1: The Fermi-Dirac distribution $f(E)$ describes to what extent the energy states of the electrons in a solid are occupied. In a material with no chemical potential they are approximately filled up to E_F , around which $f(E)$ is smeared symmetrically (more at higher temperatures) before the probability of an energy state to contain electrons goes down to zero. This is a crucial feature in the SIN and SIS' junctions, see also figures 2.3 and 2.4.

is illustrated in figure 2.1. With E measured relative to E_F in a non-doped material at a temperature T we have:

$$f(E) = \frac{1}{1 + e^{\frac{E}{k_B T}}} \quad (2.1)$$

2.2 The properties of superconductors

Superconductors have two defining properties: first, they carry current without resistance, and second, any applied magnetic field is effectively cancelled within the superconductor (SC) due to induced circular currents in the material. The second property is referred to as the Meissner effect.

There is an almost instantaneous transition in the SC resistivity at a critical temperature called T_c . Below this, the material is in the superconducting state, and above T_c the material is in the normal state. This can be presented in the simple two-fluid model of superconductivity first introduced by Gorter and Casimir in 1934 [21]. The electrons of a superconductor are divided into two fluids, one normal fluid and one superfluid. The electrons of the normal fluid behave very much like the electrons of a normal metal, while the superfluid electrons have some rather peculiar properties. Near the Fermi surface of the SC, the electron-phonon coupling, where electrons affect each other through interaction with ions, overtakes the normally dominant Coulomb interaction between electrons. This leads to the formation of so called Cooper pairs of electrons, with opposite momenta and spin, moving in the SC at the Fermi surface [22] i.e. having an internal energy equal to

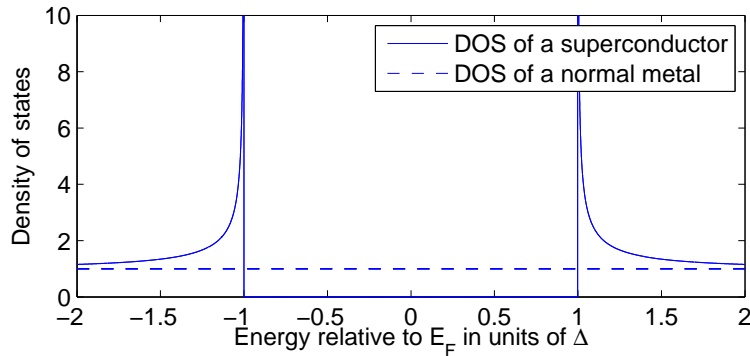


Figure 2.2: Due to the formation of Cooper pairs in a superconductor, there are no states for the electrons to occupy within an energy interval of Δ around the Fermi surface. Instead, there are more states with energies a bit further away than there is in a normal metal. The density of states (DOS) multiplied by the Fermi-Dirac distribution gives a measure of the density of electrons in the SC, see also figure 2.3.

the Fermi energy. The Fermi surface is the three dimensional equivalence of the Fermi level. As some energy is required to break a Cooper pair, there will be an energy gap $\Delta(T)$ in the SC corresponding to the breaking energy of a Cooper pair, leading to a discrepancy in the Fermi-Dirac distribution of the electron energies in the SC, see figures 2.2 and 2.3.

2.3 The SIN junction

An SIN junction consists of the boundaries between a normal metal (N), an insulator (I) and a superconductor (S). As described in the previous section, around the Fermi surface of the superconductor there is an energy gap in which no electrons can exist. As long as the Fermi surfaces of the absorber and the superconductor are aligned and the temperature is not too high, there will be no net transfer of electrons across the insulator. A small bias voltage can be applied over the junction though, raising the Fermi level of the absorber. Since the electron energies are Fermi-Dirac distributed around the Fermi surface, some of the “hot”, more energetic electrons then will tunnel through the junction to the available states in the superconductor. This is illustrated in figure 2.4.

As for the tunnelling rate, it will be the product of the number of electrons on one side of the barrier, the number of empty states at the corresponding energy on the other side of the barrier and the transparency of the barrier, integrated over all energies. Taking into account tunnelling in both

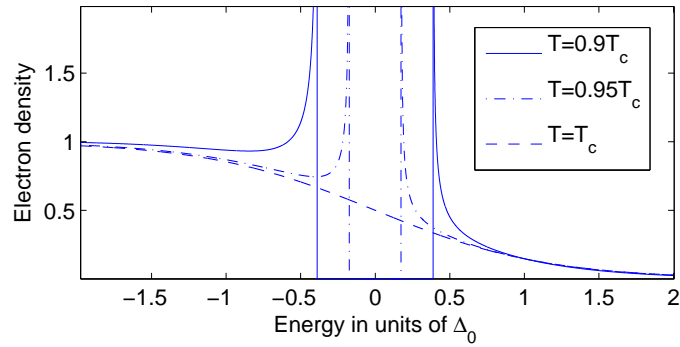


Figure 2.3: Electron density in a superconductor near T_c , plotted for $T = 0.9T_c$ and $T = 0.95T_c$, where the SC is in the superconducting state, and $T = T_c$, where the SC is in the normal state. The energy gap decreases with increasing temperature. Δ_0 is the gap at zero temperature. One unit of electron density represents a full energy state in a normal metal for each energy. Compare with figures 2.1 and 2.2.

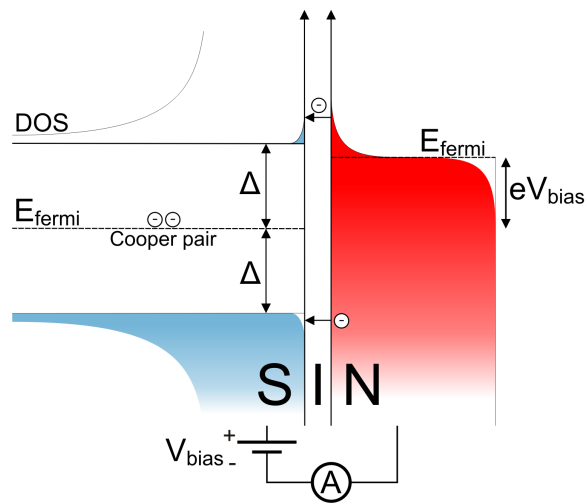


Figure 2.4: A visualization of how the electron densities allow electron tunnelling across an SIN junction at some temperature when a bias voltage V is applied over the junction. The resulting $I(V, T)$ curves are illustrated in figure 2.6.

directions, we will have a current through the barrier:

$$I(V,T) = \frac{1}{eR_N} \int_{-\infty}^{\infty} N_s(E) (f(E) - f(E + eV)) dE \quad (2.2)$$

where $N_s(E)$ is the DOS of the superconductor, e is the elementary charge, V is the applied bias voltage and $f(E)$ is the Fermi-Dirac distribution in eq. (2.1) in units of electronvolts. The factor $\frac{1}{R_N}$ is such that $I(V)|_{T=0} = \frac{V}{R_N}$ at high voltages, i.e. voltages that shift the Fermi level of the normal metal to a point where the SIN junction behaves as an NIN junction (two normal metals separated by an insulator where the Fermi level of one of the metals is slightly elevated with respect to the other). The resistance is then R_N , the resistance of the insulating barrier.

In the low temperature limit $k_B T \ll \Delta$, the factor $(f(E) - f(E + eV))$ in eq. (2.2) can be approximated by

$$f(E) - f(E + eV) \approx e^{-\frac{E}{k_B T}} \left(1 - e^{-\frac{eV}{k_B T}} \right) \quad (2.3)$$

$N_s(E)$ in turn is given by

$$N_s(E) = \frac{|E|}{\sqrt{E^2 - \Delta^2}} \Theta(|E| - \Delta) \quad (2.4)$$

with Θ being the Heaviside step function. The DOS will have a sharp peak at $E = \pm\Delta$, as shown in figure 2.2. Approximating the width of the peak with $k_B T$, the integral can be approximated using standard steepest descent techniques. The result is:

$$I(V,T) \approx \frac{1}{eR_N} \sqrt{2k_B T \Delta} e^{-\frac{\Delta - eV}{k_B T}} \quad (2.5)$$

This temperature dependence is plotted in figure 2.5 together with the exact expression given in eq. (2.2). At different temperatures, the IV characteristics of an SIN junction, $I(V)|_{T=const}$, and the current response at different bias voltages and vice versa, changes as is illustrated in figure 2.6.

2.4 The SIS' junction

An SIS' junction differs from the SIN version mainly by the fact that the normal metal part instead consists of a weak superconductor, denoted by S'. The principle is roughly the same: excited electrons tunnel through an insulating barrier, and by applying a bias voltage across the junction, it is possible to shift the Fermi levels of the superconductors to increase the tunnelling effect as is shown in figure 2.7. The shape of the IV curves depends upon the dimensions of the energy gaps of the two superconductors. When

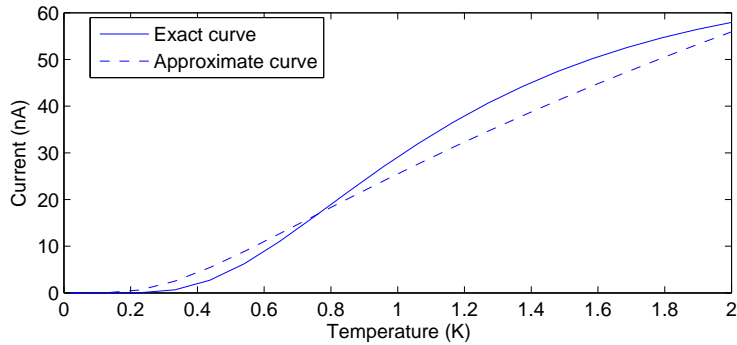


Figure 2.5: The current through an SIN tunnel junction, plotted at a constant bias voltage of $174 \mu\text{V}$ and an energy gap of $200 \mu\text{V}$. The approximated expression is given by eq. (2.5). If temperature differences are to be detected, the best response to these is given by a junction held at a bias voltage/current such that the resulting current/voltage changes as rapidly as possible with a change of temperature. See also figure 2.6.

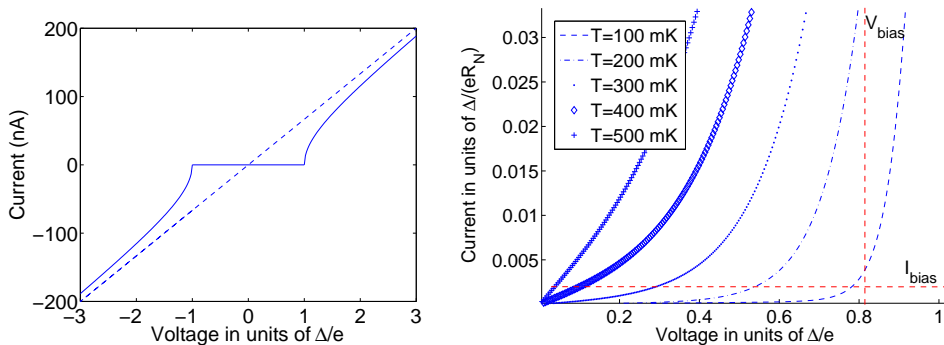


Figure 2.6: IV characteristics $I(V,T)$ for an SIN junction. To the left are the curves for $T = 0$ and $T \geq T_c$, where the latter is a straight line with a tilt equal to the normal resistance R_N of the insulator. To the right is a close-up at different temperatures. It also illustrates the current response at a bias voltage and vice versa. If a bias voltage is applied and a change in temperature takes place, the current will have to change along the dashed line which is marked with V_{bias} . Compare with figures 2.5 and 2.4. [23]

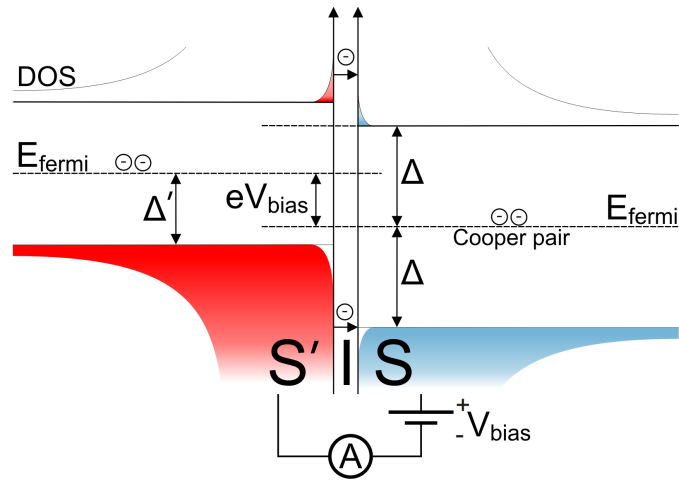


Figure 2.7: Visualization of how the electron densities allow electron tunnelling across an SIS' junction at some temperature when a bias voltage V is applied over the junction. The IV characteristics are shown in figure 2.8.

no bias voltage is applied, all components' Fermi energies, and therefore also their band gaps, are aligned. Cooper pairs exist only at the Fermi energy and they flow freely through the insulator, giving rise to a Josephson current, as is illustrated with the IV characteristics in figure 2.8. At bias voltages an oscillating Josephson current will also be present due to the properties of superconductors, although it is not shown in the figure.

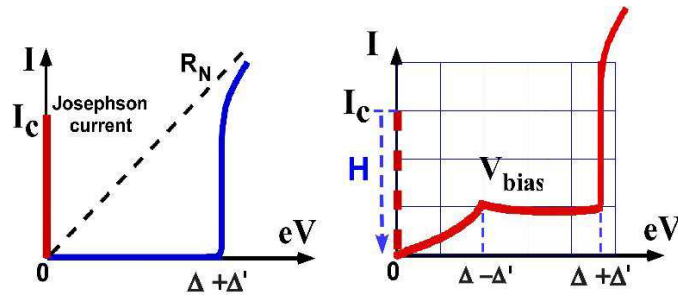


Figure 2.8: IV characteristics for an SIS' junction at $T \approx 0$ K with and without suppression of the Josephson current I_c , which can be done by applying an external magnetic field. At higher temperatures, the IV curves will gradually approach a normal resistance R_N . In the case when S' is a weaker superconductor than S, $\Delta > \Delta'$, the process will include the features of the SIN junction IV characteristics once the S' becomes a normal metal. Picture from [23].

Chapter 3

The Cold-Electron Bolometer Concept

The Cold-Electron Bolometer concept is based on the fact that electrons in a piece of metal heated by radiation may tunnel through an SIN or SIS' junction, producing a current or voltage that can be measured; the feature where the hot electrons are removed is the cold-electron effect. However, the concept also includes how the pieces are put together to end up as parts of a highly sensitive device. This chapter begins by explaining how the CEB works in its simplest form, and by showing a simulation of how it comes to do so. Thereafter the BOOMERanG requirements and the current development lines for the CEB are presented, together with some theory describing how the bolometers meet with the NEP requirements. We then look at what can be expected from a decrease in absorber volume. The chapter ends with a section on how the bolometer parts are arranged on chip.

3.1 The CEB in working mode

A CEB measures incoming electromagnetic radiation and consists of different metal structures placed on a substrate made of e.g. silicon. The electromagnetic waves are captured by antennas and led through capacitively coupled junctions to the absorber (N or S') where the photon energy is transferred to electrons. The excited (hot) electrons may then tunnel across one of the junctions connected to the absorber as shown in figure 3.1. The resulting current and voltage, in the ideal case proportional to some power of the incoming radiation, may be measured and analysed.

3.1.1 The cold-electron effect

The excited electrons in the absorber may be relaxed due to electron-phonon coupling, thereby converting their kinetic energy to heat. In short: the larger

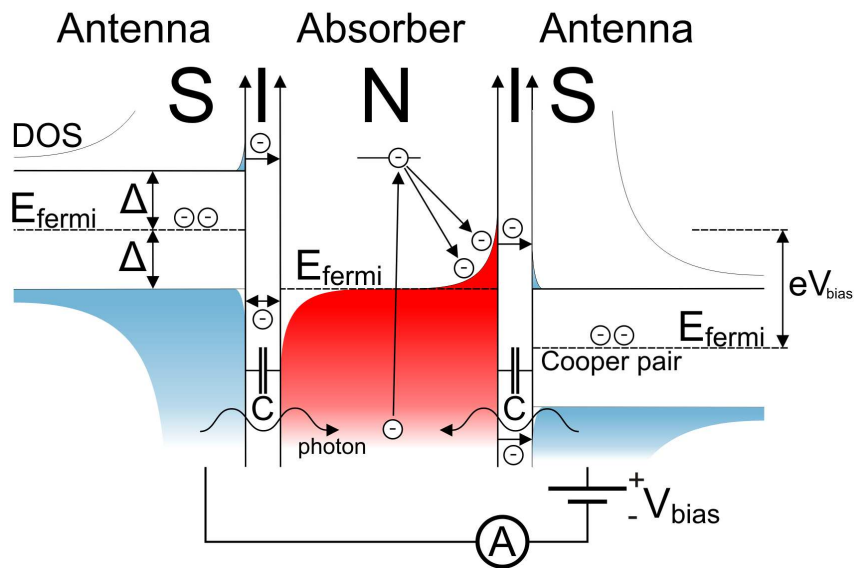


Figure 3.1: A visualization of an SIN tunnel junction in a CEB. Electromagnetic radiation crosses the capacitively coupled junctions from the antennas to the absorber. There, the energy of a photon is transferred to an electron. A bias voltage/current applied over the two junctions enables the hot electron to tunnel across one of the SIN junctions, creating a measurable current/voltage. Ideally though, the distance from the excited electron to the tunnel junction is large enough for the energy of the first hot electron to be divided between several other electrons. Even when that is not the case, there is still a rather high probability of the hot electron to be detained long enough by the insulating barrier. This increase of hot electrons gives rise to an increase in the resulting current and voltage. The hot electron transfer across the junction yields an additional benefit: the absorber has an intrinsic cooling mechanism, since the high energy electrons are constantly removed.

the thermal conductance across the tunnel junction, G_{cool} , is in comparison with the thermal conductance between the electron and phonon subsystems G_{e-ph} , the more electrons will tunnel. We will investigate this in terms of relaxation times: the estimated time between two tunnelling events τ_{cool} and the estimated time between two relaxation events in the absorber τ_{e-ph} . Ideally the relaxation time for the tunnel junction is significantly lower than the corresponding time for the electron-phonon system, since $\tau \propto G^{-1}$ as is shown below.

The parameters determine the electron-phonon relaxation time are how easily heat is transported from electrons to phonons, i.e. G_{e-ph} , and the amount of thermal energy available in the electron gas, the electronic heat capacity C_e . The relaxation time is then

$$\tau_{e-ph} = \frac{C_e}{G_{e-ph}} \quad (3.1)$$

The electronic heat capacity is given by the well known formula

$$C_e = \gamma V T_e \quad (3.2)$$

where V is the volume and γ the Sommerfeld constant [19]. With N being the electron density, k_B the Boltzmann constant and T_F the Fermi temperature, the latter is given by:

$$\gamma = 2\pi^2 \frac{N k_B}{T_F} \approx 3.7 \times 10^{-16} \text{ J/K}^2 \mu\text{m}^3 \text{ for Al} \quad (3.3)$$

As for the thermal conductance, the expression is more elusive. Experimental results indicate that G_{e-ph} is proportional to some power of the electron temperature T_e . In [24], $G_{e-ph} \propto T_e^4$ was proposed, while Agulo [25] found that $G_{e-ph} \propto T_e^5$ gave a better fit to his experimental data on Cold-Electron Bolometers. In our simulations, the former results have been used, although both models mentioned yield similar results. The thermal conductance is then given by

$$G_{e-ph} = 5\Sigma V T_e^4 \quad (3.4)$$

where V again is the volume of the absorber and Σ is a constant of the material, experimentally determined to be $2 - 3 \text{ nW}/\mu\text{m}^3 \text{K}^5$ for Al [26]. The resulting relaxation time is then

$$\tau_{e-ph} = \frac{\gamma}{5\Sigma} T_e^{-3} \quad (3.5)$$

To find τ_{cool} we continue in the same fashion as for τ_{e-ph} , writing

$$\tau_{cool} = \frac{C_e}{G_{cool}}, \quad G_{cool} \equiv \frac{\partial P_{cool}}{\partial T_e} \quad (3.6)$$

where P_{Cool} basically is the power dissipated in the tunnel junction [26]:

$$P_{cool} = I \cdot V \stackrel{\text{eq. (2.2)}}{=} \frac{1}{e^2 R_N} \int_{-\infty}^{\infty} EN_s(E) (f(E) - f(E + eV)) dE \quad (3.7)$$

To calculate the relaxation times, we need the electron temperature. In order to find this, we consider energy conservation in the bolometer. The energy transfer to the electron subsystem is mainly due to an external powerload, P_0 , Joule heating of the absorber, $I^2 R_{abs}$, heating due to back-tunnelling electrons through the junction, $\beta \frac{I}{e} \Delta$ (β is the reabsorption coefficient, i.e. the fraction of electrons that back-tunnel), and power dissipation in the subgap region, V^2/R_s . The subgap region and R_s are explained in more detail in section 5.2.1. The energy transfer out of the electron subsystem is due to the heat flow P_{e-ph} between electrons and phonons and the removal of hot electrons through the tunnel junction, i.e the cold-electron effect [25]:

$$P_{cool} + P_{e-ph} = P_0 + I^2 R_{abs} + \beta \frac{I}{e} \Delta + \frac{V^2}{R_s} \quad (3.8)$$

In real working mode, the electron temperature will essentially be determined by the external powerload. Moreover, P_{e-ph} is obtained by integrating the thermal conductance over the electron temperature and using the fact that when the electrons and phonons are in thermal equilibrium there will be no heat transfer between them:

$$P_{e-ph} = \Sigma V (T_e^5 - T_{ph}^5) \quad (3.9)$$

The electron temperature can now be simulated with eq. (3.8); this is shown in figure 3.2. In this and all following simulations in this chapter, the small heating due to the back-tunnelling electrons has been considered to be negligible and the following parameters have been used:

$$\begin{aligned} V &= 0.02 \mu\text{m}^3 \\ R_N &= 3 \text{ k}\Omega \\ R_s &= 7 \text{ M}\Omega \\ R_{abs} &= 60 \Omega \\ \Delta &= 200 \mu\text{eV} \\ \Sigma &= 2 \text{ nW}/(\mu\text{m}^3 \text{K}^5) \\ \gamma &= 3.7 \times 10^{-16} \text{ J}/(\text{K}^2 \mu\text{m}^3) \end{aligned}$$

Using the obtained electron temperatures, the electron-phonon relaxation time is simulated and plotted in figure 3.3. Finally, the ratio between the relaxation times at a working temperature of 300 mK, see also section 3.2, is shown in figure 3.4. We see that the electrons may tunnel through the junction much sooner than interacting with the surrounding phonons, which is exactly what we anticipated.

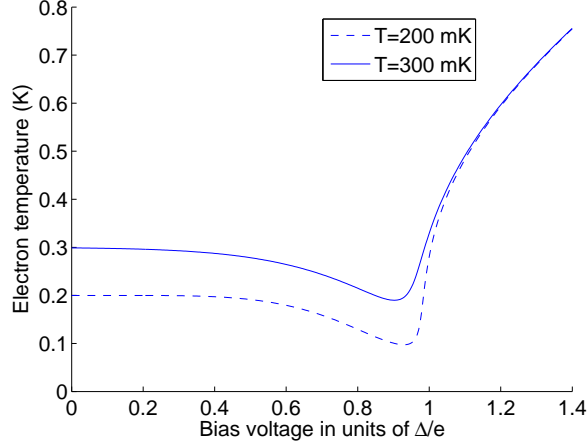


Figure 3.2: Electron temperatures in a CEB at two different phonon temperatures, plotted as a function of bias voltage normalized to the energy gap. We see that the decoupling of the phonon and electron subsystems is strongest in a region near Δ/e , where the heat transfer between the two subsystems is at its lowest.

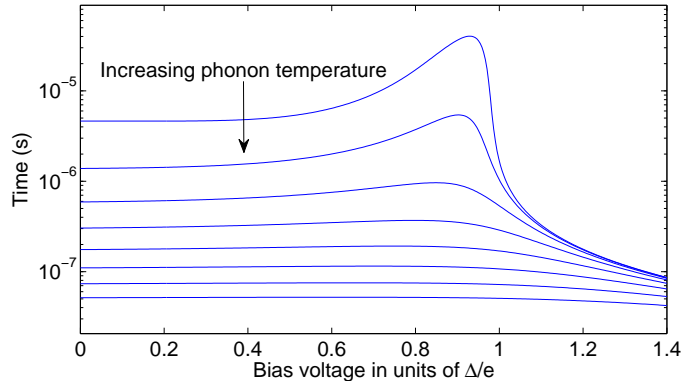


Figure 3.3: The electron-phonon relaxation time as a function of bias voltage at temperatures ranging from 200 mK to 900 mK. The higher τ_{e-ph} , the more prone the electrons will be to tunnel rather than give off energy to the phonon subsystem. We clearly see that the decoupling of the two subsystems decreases with increasing phonon temperature, and that it is strongest in a region near Δ/e . See also figure 3.2.

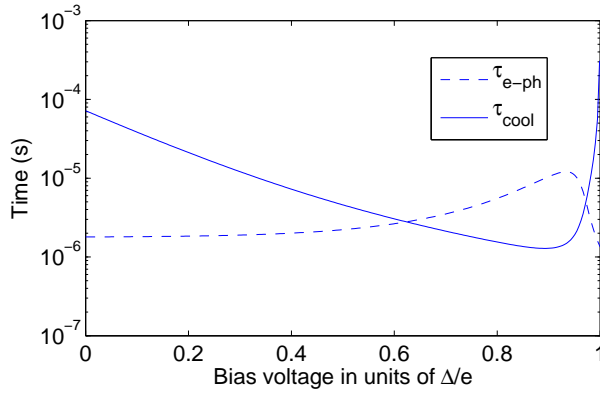


Figure 3.4: The tunnelling relaxation time τ_{cool} and the time between two energy relaxation events τ_{e-ph} for hot electrons in a normal metal absorber versus bias voltage. The higher the value of τ_{e-ph}/τ_{cool} , the more inclined the electrons are to tunnel rather than lose their energy to the absorber phonons. This ratio is generally a bit worse for simulations plotted as a function of bias currents. For bias voltages however, we clearly see that the best operating point is with voltages relatively close to Δ . Since $G_{cool} > G_{e-ph}$ ($\tau \propto G^{-1}$) is enough for the electrons to tunnel rather than lose their energy when voltage bias mode is used, we also see that it is probable that the energy loss is small at these operating points. Also, as shown in eq. (3.6), τ_{cool} is directly proportional to the volume. Thus, less absorber volume means a larger decoupling of the two subsystems and a faster response to incoming radiation.

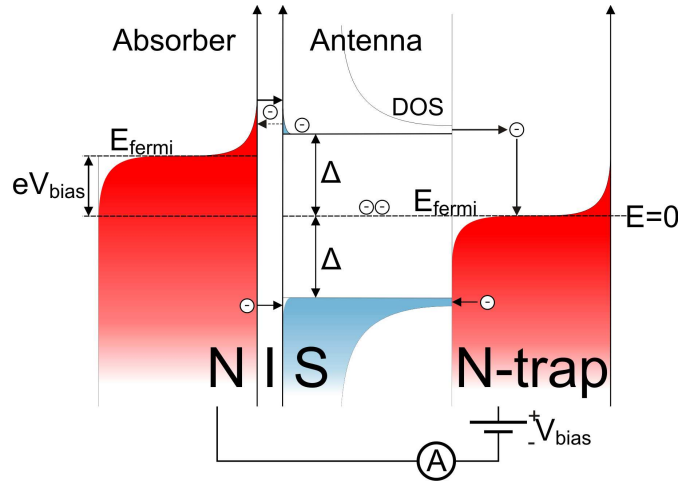


Figure 3.5: A visualization of a SIN junction with a normal metal trap which captures the hot electrons that have tunneled through the junction and removes the danger of them back-tunnelling across the junction. [23]

3.1.2 Prevention of back-tunnelling

Once the hot electrons have tunneled through the junction, there is a risk of them back-tunnelling from the SC to the absorber, thus decreasing the current across the junction which is caused by the incoming radiation. To avoid this, there are two possible measures to be taken. Firstly, one can increase the volume of the SC, to allow for the tunneled electrons to diffuse out into the SC. Secondly, as is shown in figure 3.5, an electron trap can be introduced at the far end of the SC to deposit the high energy particles [25]. The electron trap simply consists of a piece of normal metal, placed at the far end of the antenna. Typically, a rather thick layer (~ 600 nm) of Au is used. [27] [28]

3.1.3 Voltage and current biasing

There are two different working modes for the CEB: current bias mode and voltage bias mode. As is illustrated in figure 2.6, either the current or the voltage across the junction is kept at a constant value while the response to incoming radiation is measured as change in the other parameter. The best values to use for the I_{bias} and V_{bias} are those where an increase in the electron temperature, at the temperature the CEB is to work at, brings as large a change in voltage or current as possible. For voltage bias mode, this is at a V_{bias} slightly smaller than $\frac{\Delta_0}{e}$, and for I_{bias} , the resulting voltage at the working temperature should be around $\frac{\Delta_0}{2e}$.

However, there is a fundamental difference between the two modes. Since the current is kept at a constant value in the current bias mode, the cold-

electron effect, where the hot electrons are removed from the absorber, is suppressed. As a result, the voltage bias mode is better in all physical senses, as is described in figure 3.4. The fact that it requires larger areas of the tunnel junctions is not a problem with the current manufacturing technique described in figure 4.1. There are some practical problems though, so we have used current bias mode for all our work.

A readout of an SIN junction bolometer is done using a superconducting quantum interference device (SQUID), due to its high dynamic range, whereas the readout of an SIS' junction bolometer can be done with a JFET or MOSFET amplifier.

3.2 BOOMERanG requirements

The requirements of the BOOMERanG project effectively summarise the demands the CEB currently is in progress to meet with: bolometers with JFET readout for 92 channels, with a noise equivalent power (NEP) less than the photon noise at an optical powerload of 5 pW, and a resolution of B-polarization better than 20 dB. The operating temperature should be around 300 mK.[16]

The requirements concerning the number of channels and polarization measurements is a matter of the number of bolometers used for the final measurements and the arrangement of the antennas of the bolometers, so that different polarizations of the incoming radiation can be measured apart from each other. The NEP on the other hand is a measure of the minimal detectable output of the device at a certain bandwidth. The desire is that this should be limited by the photons rather than the measurement device, i.e. the bolometer.

When the accuracy of the measurement of the incoming radiation is to be better than the uncertainty of the energy brought there by the photons, the CEB naturally needs to respond excessively to radiation. The readout of an ordinary two-junction bolometer with one absorber, e.g. the one in figure 3.1, simply isn't up to the challenge. Improvements of the system are vital, and can be done by e.g. decreasing the absorber volume, as mentioned before. Another way of increasing the so called sensitivity of the CEB is to connect several absorbers with junctions in an array, so that the voltage/current from each junction contributes to a total resulting voltage/current. This is especially desirable for SIN junctions, as the dynamic resistance of an SIN array can be matched with a JFET amplifier.

3.3 An array of SIN junctions

Recently, the Bolometer group at Chalmers started utilizing arrays of SIN junctions. Intuitively, an array of N absorbers with their respective junctions

will yield N times the response from just one absorber, exactly compensated by the division of the external powerload between the absorbers. However, this is not the whole story. For a single absorber, an external power source could overheat it, making it less sensitive to radiation. Dividing the power over several absorber lowers the risk of overheating them, meaning that the bolometer as a whole will work with much improved characteristics. This is a very advantageous feature for a CEB, and the reason why the ARRay structures (abbreviated ARR later) is a line in the CEB concept.

The ARRay structures currently have their absorbers connected in series since the parallel version brings some complications. This means that read-outs of the system must be made in current bias mode to have the desired feature described above, even though voltage bias mode would be preferable. Another drawback is that the NEP is increased in the same way as the response, i.e. approximately \sqrt{N} times (see also section 3.5). Hence a decrease of the absorber volumes is necessary, decreasing the NEP and increasing the sensitivity at the same time.

For smaller absorber volumes, the type of metal or metals used for the structure in question becomes important. The T_c should remain below the convenient operating and testing temperatures (50-300 mK) so that the absorber consists of a piece of normal metal. One way to regulate the T_c is to have a thin layer of chromium below a thick layer of aluminium as the absorber. The thicknesses are then important parameters, for the presence of Cr destroys the tendencies to superconductivity of Al. The safest way of decreasing the absorber volume is therefore to decrease the thickness of the Al layer. Previous studies have shown that an alloy of a 20 nm layer of Al on top of a 0.5 nm layer of Cr retains the properties of a normal metal down to the cryogenic temperatures the CEB operates at. [13]

3.4 SIS' lines of development

The SIS' junction bolometer has the advantage of managing JFET readout in voltage bias mode. Here, as for the ARRay line of development in section 3.3, smaller absorber volumes are desired. Instead of only decreasing the aluminium thickness in the absorber, the chromium thickness also needs to be decreased until the absorber shows S' features at temperatures slightly below 100 or 300 mK.

The lines of development are the BOOMerang and the FINline structures, and the main differences from the ARRay structure are the shape of the single junction and the shapes of the antennas, which are described in section 3.7. For a more in-depth explanation, figure 3.7 is a good starting point. When no bias voltage is applied over the absorber and its two junctions, all components' Fermi energies are aligned. The Cooper pairs, existing

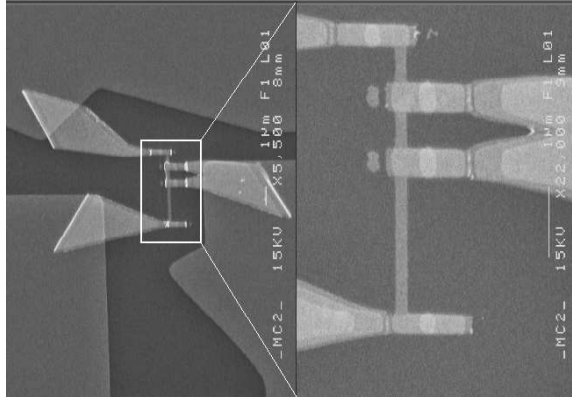


Figure 3.6: An illustration of the loop geometry used in SIS' junctions. The picture shows the absorber as the vertical line, the junctions as the horizontal lines and is taken with an SEM microscope, see section 4.6.2. The loop geometry which suppresses the Josephson current at zero bias voltage consists of the structure to the right in the magnified picture: two junctions connected to each other, forming a loop with a piece of the absorber. When an external magnetic field is applied over the loop in the right way, a current opposite to the Josephson current is induced. [10]

only at the Fermi energy, then flow freely through the insulator, giving rise to a Josephson current (see also figure 2.8). This is a problem when doing measurements on the IV characteristics of the junction, for they are done in current biased mode, and the sweep of the current then skips a bit of the IV characteristics.

Because of this, the current needs to be suppressed in order to make sensitive measurements. This can be achieved by a so called loop geometry which is shown in figure 3.6, a concept developed by Leonid Kuzmin where an induced current negates the Josephson effect at the point of measurement [10].

The IV characteristics of the SIS' junction (figure 2.8) will also clarify the next quirk used in the superconducting CEBs. The weak superconductor, the absorber, is initially held at a temperature just below the critical temperature. During the transition to a slightly higher temperature, above T_c where the absorber is a normal metal, the IV dependence will go from SIS' to SIN. Because the transition between normal and superconducting metal is continuous and very quick, a small heating equivalent of a single photon will significantly change the current if the bias voltage is set correctly. The best responsivity is achieved when the operating point is in the area between $\Delta - \Delta'$ and $\Delta + \Delta$ in figure 2.8, where the difference between the characteristics of an SIS' and an SIN junction is as most pronounced. In some parts of this region, the dynamic resistance is so low that it would

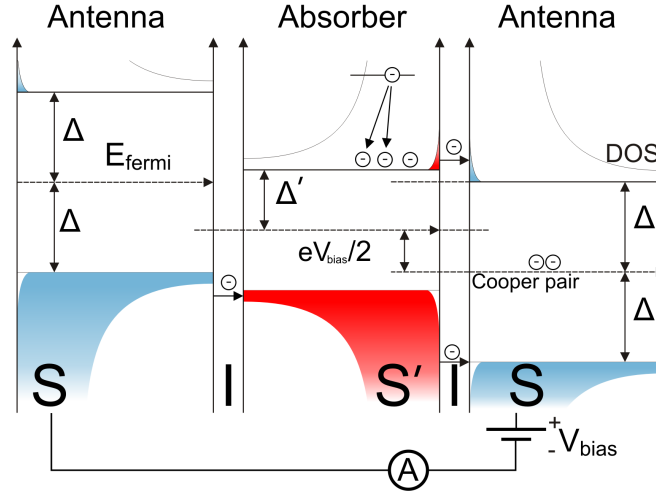


Figure 3.7: A visualization of the SIS' bolometer, which more accurately is an SIS'IS bolometer since both ends of the absorber are used for tunnelling. As the bias voltage is increased, the Fermi level of the superconductor in the middle is raised, and when the applied bias voltage causes the upper parts of the gaps to align, the current through the junction will peak. Compare with the IV characteristics in figure 2.8. [23]

be negative if there were no smearing of the IV curves, ordinarily due to $T \neq 0$ and haphazardly scattered metal around the junctions. Anyway it is possible to choose an operating point with the same impedance as, or very close to, that of the JFET, thus minimizing the noise.

3.5 Noise equivalent power

We have already mentioned one parameter of interest in the bolometer, namely the responsivity, being a measure of the change in output due to applied power. The second characteristic parameter of the bolometer is Noise Equivalent Power (NEP). By definition, it is “*the power that produces a signal-to-noise ratio of unity of a given optical detector at a given data-signalling rate or modulation frequency, operating wavelength, and effective noise bandwidth*” [25]. It is a measure of the minimal detectable output of the device at a certain bandwidth. There is an inevitable contribution to the noise from the photons themselves: due to the Heisenberg principle their energy cannot be exactly determined. We can write:

$$\text{NEP}_{tot}^2 = \text{NEP}_{ph}^2 + \text{NEP}_{meas}^2 \quad (3.10)$$

If the NEP of the bolometer is lower than the NEP for the photons, the limitation on the device is the inevitable photon noise. This has actually

been accomplished using both an array of SIN-type bolometers and a single SIS'-type bolometer [11][10].

The NEP of the measuring device can also be divided into some major contributions: Noise in the SIN/SIS' junction, $NEP_{junction}$, noise due to heat flow between electrons and phonons, NEP_{th} , and the noise of the amplifier. The first two of these contributions collectively constitute the bolometer NEP:

$$NEP_{meas}^2 = NEP_{bol}^2 + NEP_{amp}^2 \quad (3.11)$$

This subdivision is reasonable since both the NEP of the measuring device and the NEP of the amplifier can be measured, and the NEP of the bolometer can be extracted using eq. (3.11). We will now investigate each of those contributions, in the end resulting in expressions for all the contributing terms. We first consider the photon noise.

3.5.1 Photon noise

Under the assumption that the radiation received by the bolometer is essentially thermal, the energy distribution of the incoming photons is described by the Bose-Einstein distribution:

$$n(f,T) = \frac{1}{e^{\frac{hf}{kT}} - 1} \quad (3.12)$$

where T is the temperature of the radiating black-body, h is Planck's constant and f is the frequency of the radiation. The photon noise is due to the fluctuation of the number of incoming photons in a given bandwidth. Using basic statistical mechanics [29] we obtain for the fluctuation per second:

$$\langle (\Delta n)^2 \rangle = \langle n^2 \rangle - n^2 = \frac{kT}{h} \frac{\partial n}{\partial f} = n(n+1) \quad (3.13)$$

Moreover, the power received in a frequency interval df is:

$$P(f,T)df = hf n(f,T)df \quad (3.14)$$

where T is the temperature of the radiating body and k is the Boltzmann constant. For $hf \ll kT$ we can do a Taylor expansion of the denominator in the Bose-Einstein distribution, giving:

$$P(f,T)df = kTdf \quad (3.15)$$

Now the variance of the incoming power for a detection band B per second will be:

$$\begin{aligned} \langle (\Delta P)^2 \rangle &= \int_B h^2 f^2 n(n+1)df = \int_B P(f,T)hf + P^2(f,T)df \approx \\ &\approx kT(hf_0 + kT)B \end{aligned} \quad (3.16)$$

The NEP squared will be twice this number, since a one second unweighted average correspond to a detection bandwidth of 1/2 Hz. Our bolometers will operate at 300 GHz with a bandwidth of 50 GHz. Taking into account the absorptivity of the bolometer we obtain a photon noise of $\text{NEP}_{ph} \approx 5 \times 10^{-17} \text{ W/Hz}^{1/2}$. [26]

3.5.2 Thermal (electron-phonon) noise

There is an inevitable noise contribution originating in the quantization of the energy transfer between the absorber and the substrate. For systems in thermal equilibrium, there is a classical thermodynamical result [31]:

$$\text{NEP}_{th}^2 = 4kT^2G \quad (3.17)$$

where G is the heat conductance. However, one main feature of our bolometers is that the electrons are at a different temperature than the phonons. The expression is then modified to [32]:

$$\text{NEP}_{th}^2 = 2kT_e^2G_e + 2kT_{ph}^2G_{ph} \quad (3.18)$$

With the result for the heat conductance mentioned earlier, we have:

$$\text{NEP}_{th}^2 = 10kV\Sigma(T_e^6 + T_{ph}^6) \quad (3.19)$$

We note the enormous temperature dependence. From this term, it should be obvious that a low electron temperature and measurement temperature will have a profound effect on the noise in the bolometer.

3.5.3 Noise in the junction

We now turn to the noise in the junction. This noise actually has two separate contributions: firstly, the quantization of the charge transfer (the tunnelling electrons) will give rise to a shot noise, and secondly, the electrons carry heat; thus also thermal noise will be important.

Near the optimum bias point, we can use the following well known expression for the shot noise (see e.g. [32]):

$$\langle \delta I_\omega^2 \rangle \approx 2eI \quad (3.20)$$

which is a result also obtained by considering (2.5). As for the heat flow noise $\langle \delta P_c^2 \rangle$ we have from [26]:

$$\langle \delta P_c^2 \rangle = \left[\left(\ln \left(\frac{\sqrt{2\pi\Delta kT}}{2e|I|R_N} \right) \right)^2 + \frac{1}{2} \right] \frac{k^2 T^2}{e} |I| \quad (3.21)$$

There is obviously a correlation between these contributions, and this correlation will also affect the noise. The correlation is approximately $\langle \delta P_c \delta I_\omega \rangle \approx 2eP_c$. The total expression for the noise is then [26]:

$$\begin{aligned} \text{NEP}_{SIN}^2 &= \frac{\langle \delta I_\omega^2 \rangle}{S_V^2} \left(\frac{\partial V}{\partial I} \right)^2 + \langle \delta P_c^2 \rangle + 2 \langle \delta P_c \delta I_\omega \rangle \frac{1}{S_V} \frac{\partial V}{\partial I} \approx \\ &\approx \frac{2eI}{S_V^2} \left(\frac{\partial V}{\partial I} \right)^2 + \left[\left(\ln \left(\frac{\sqrt{2\pi\Delta kT}}{2e|I|R_N} \right) \right)^2 + \frac{1}{2} \right] \frac{k^2 T^2}{e} |I| + \\ &\quad + 2 \frac{(2e|I|) \ln \left(\frac{\sqrt{2\pi\Delta kT}}{2e|I|R_N} \right)}{|S_V|} \frac{\partial V}{\partial I} \end{aligned} \quad (3.22)$$

where $S_V = \frac{1}{G} \frac{\partial V}{\partial T}$ is the responsivity in current biased mode.

3.5.4 Amplifier noise

The readout system for our bolometers will be a JFET or MOSFET transistor, the intrinsic noise of which will also add to the total noise. The contribution can be expressed in terms of the responsivity S_V , the voltage noise e_n , the current noise i_n and the dynamic resistance R_d :

$$\text{NEP}_{amp} = \frac{e_n^2 + (i_n \sum R_d)^2}{S_v^2} \quad (3.23)$$

3.6 Expectations of a decrease in absorber volume

The expected effects of implementing a thinner absorber in the CEB concept are several. The absorber is the most critical part of the bolometer and a decrease of its volume affects how it reacts to an external powerload (how soon the excited electrons tunnel across the junction). The decrease may be done in three dimensions: width, length and height.

How narrow and short the absorber can be is limited by the manufacturing process and the design of the junctions. A too narrow absorber simply results in no absorber at all due to limitations of the e-beam lithography and the development used during fabrication. Too short absorbers is not a good idea either, for the shorter the way to the junctions, the less probability for the energy of a photon to be divided between several electrons. This leaves the height, and a problem with a decrease of the height of the absorber is that the superconducting properties of large ‘‘bulk’’ materials are different from thin layers of the same. It is difficult to make predictions concerning T_c and Δ in thin films.

The advantages of a smaller volume are many though. The thermal conductance G_{e-ph} between electrons and phonons, presented in eq. (3.4), is

directly proportional to the volume, so a lower G_{e-ph} means a larger decoupling of the electron-phonon subsystem, and thus a more efficient electron cooling. The NEP in turn is inversely proportional to a power of G_{e-ph} . Hence, a decrease in the NEP is expected when the absorber volume is decreased. However, the effect on NEP can in fact be larger because of the increased electron cooling. This acts to lower the conductance even more, since it has a very large temperature dependence, which is why optimizing our absorbers to work in their optimal mode at the desired operating point can have a profound impact on the NEP. In short: less volume increases the response to radiation; more electrons tunnel as a result of the same amount of incoming radiation. This also works the other way, for the smaller the absorber volume, the less powerload is needed to overheat the absorber.

Moreover, there is a suspicion that smaller absorbers can lead to a lower leakage in the junction, partly due to less scattering of conducting material during the evaporation process, as was previously mentioned. More importantly, when the absorber's aluminium is oxidized to create the tunnel junction, the thin layer of underlying chromium will probably remain unoxidized, possibly inducing leakage in the junction. Decreasing the thickness of the chromium layer could thus lead to a lower risk of leakage.

3.7 Layout of the CEB on chip

The complete structure of a CEB fits on a 7×7 mm chip, but the parts seen by the incoming radiation take up no more than $\frac{1}{25}$ of the chip area. This area is in the very centre of the chip; there, the antennas are placed. Each of the antennas is connected with a bolometer structure (one or several absorbers and tunnel junctions) placed inside the antenna structures.

From the bolometer structures, connections go in the form of wires to so called contact pads, both components made of Au. The delicate junctions are protected from electrical interferences by on-chip resistances. They are made of long trails of Ti and Pd, and have approximate values of $2 \text{ M}\Omega$ or $150 \text{ k}\Omega$.

The 16 contact pads constitute the interface between the bolometer chip and electronic apparatus. They allow for a wide range of measurement setups, such as are described in section 5.1. Several pads serve multiple purposes as most chips have additional structures for testing response and development parameters.

The CAD pattern used for chips with the ARR4 design is shown in figure 3.8. The contact pads, the wires, the resistors and the antenna can be seen clearly. However, the bolometer structure itself is too small to be distinguished. In figure 3.9 a schematic drawing of the connections between the resistors, the contact pads and the bolometer structures on the ARR4 chip is displayed.

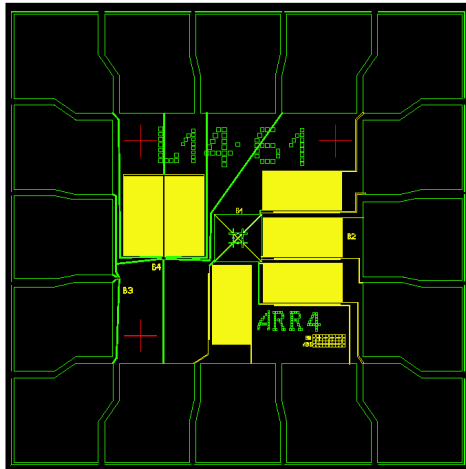


Figure 3.8: The layout of the ARR4 chip. The areas enclosed by green lines (the contact pads, some wiring connected to the contact pads and the cross-slot antenna in the middle) are all filled with Au. The antenna, at the heart of which four arrays of SIN junctions are placed, is shown in more detail in figure 3.11. The yellow rectangles are in fact many thin lines of Ti and Pd going back and forth to form the resistors. The grid in the lower right corner contains unconnected test structures with different e-beam exposure. There are also two bolometer structures, B3 and B4, on the left side of the chip. They are not connected to the antenna, but can be used for measurements to evaluate the quality of the junctions. Finally, the red crosses in the corners are used for alignment of the e-beam lithograph during the fabrication process.

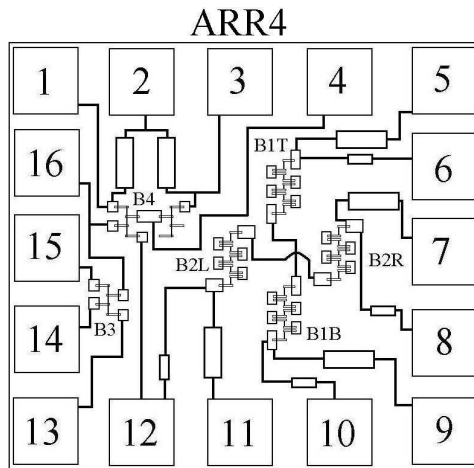


Figure 3.9: A simplified picture of the ARR4 layout. The numbers on the contact pads are the ones used during the electronic measurements on a bolometer sample. Each of the four arrays in the cross-slot antenna (B1T, B1B, B2R and B2L) is connected to one large and one small resistor. The connection between the B1 structures is separated from the connection between the B2 structures by a capacitance.

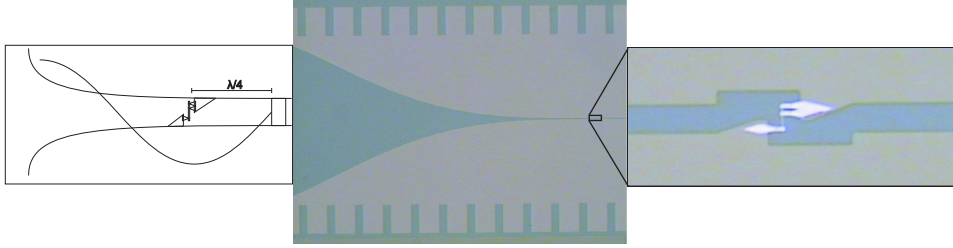


Figure 3.10: FINline antenna: By using a finlike shape (middle figure), standing waves are produced and response is increased by putting the junction in an anti-node as is illustrated in the left figure. The two parts of the antenna are connected to different contact pads. Note that the bolometer junction is made with loop geometry to suppress critical current (right). This means it is intended to be an SIS' junction.

3.7.1 Antennas

The shape and size of the antennas are crucial. In order to capture the incoming radiation well, they by rule have a size $\sim \lambda$, the wavelength of the radiation which is to be measured. Their shape on the other hand determines both how well the desired radiation can be measured and how little unwanted radiation will interfere. The antenna shape used on the FINline chips, see figure 3.10, is one way to achieve the goal of filtering out the unwanted wavelengths.

To measure B-polarization of incoming radiation however, two perpendicular pairs of interconnected triangular antennas are used. This cross-slot antenna is shown in figure 3.11. Together the triangles form a rectangular piece in the centre of the bolometer chip, guiding photons to bolometer structures at the innermost edges of the triangles. The triangular shape allow for good photon absorption as the antennas fit nicely together, and is currently a part of the ARRay structure. As these antennas have to be connected in pairs to form a circuit, each to the opposite antenna, the problem with crossing conductors has to be solved. In our case the two conductors are separated by oxidized aluminium. This technique can also be used for insulating the edges of the antennas which lie very close to each other as a result of the tight fit, removing the risk of interaction between the different antennas.

There is also another antenna configuration suitable for polarization measurements. It is the circular waveguide, shown as a part of the CAD layout for BOOM in the picture on the front page. Just like the cross-slot antenna it utilizes four bolometer structures placed to measure the horizontal and vertical components of the radiation separately.

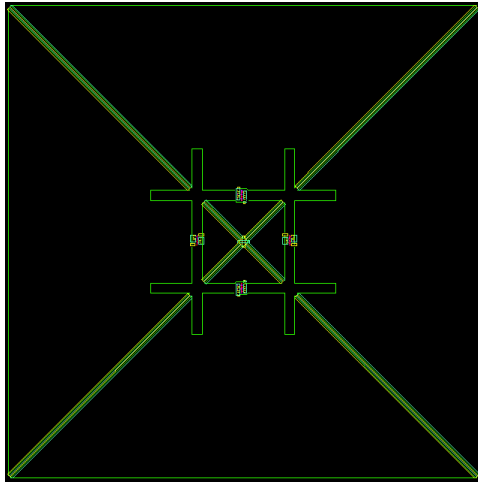


Figure 3.11: The cross-slot antenna used in ARR4. Each of the big triangles capture radiation and guides it to the corresponding bolometer structures (arrays of SIN junctions), which bridges the gap to the smaller triangle. The space between the four triangles is filled with strips made of Al and Ti/Pd respectively. The Al is evaporated first and is oxidized before the Ti/Pd layer is deposited. The oxide layer gives a capacitive coupling between the antenna triangles. In the very centre, the left and the right triangles are connected by an Al strip. The top and the bottom triangles are connected with a Ti/Pd strip, which is insulated from the Al by the aforementioned oxide layer. These connections make polarization measurements possible.

Chapter 4

The Manufacturing Process

To manufacture CEBs is a delicate task. The fabrication takes place in a cleanroom environment and consists of several steps, all of which will be explained below. Essentially a pattern is etched on a layer of resist on a substrate and through this the metal structures can be evaporated. Afterwards the resist can be lifted off, leaving the relevant structures upon the wafer. These basic steps are repeated three or four times in order to:

1. Deposit contact pads, wires and antennas, made of thick Au covered by a thin Pd layer, on the chips.
2. Deposit the resistors made of “thin gold” (Ti and Pd). For the ARR4 structure (used on wafer L14) this is the third layer; the second layer is Al which will oxidize and form a capacitance with the thin gold.
3. Deposit the bolometer structure itself.

The detailed recipes with all parameters for the wafers can be found in appendix A.

4.1 Spinning of resist

The first step of the process is to spin resist on the substrate wafer. The thin 2” wafer is made of silicon or oxidized silicon; it provides space for 36 chips. A thin layer of resist is dripped on the whole wafer, which is then spun at a speed of a few thousand rpm. This distributes the liquid across the wafer in an even layer with a thickness of less than $1\ \mu\text{m}$. The wafer is then placed on a hotplate, baking the resist for a few minutes. This attaches the resist to the wafer and gives it the desired hardness.

The process is repeated twice to give two different layers of resist. The first layer is called lift-off resist; the second is called photoresist. The use of each layer is explained in the sections below.

4.2 E-beam lithography, postbaking and scribing

To transfer the CAD pattern of the chip layout (shown in section 3.7) onto the chip itself, electron beam lithography is used. The wafer is placed in a vacuum chamber and a beam of electrons is focused upon it, moving to trace out the pattern. The electrons soften the parts of the photoresist they hit, preparing it for development. When the lithography is done the wafer usually is postbaked in an oven or on a hotplate for 10 – 20 min.

After the lithography process has been completed for the last fabrication layer, before the bolometer structure is to be deposited, the wafer is divided into individual chips. This is done using a diamond scribe. The optimal parameters for development, evaporation and lift-off can then be investigated using samples of one or two chips at a time.

4.3 Development

Once the lithography is done it is time to develop the two resist layers. This means bathing the chip(s) in chemicals which can dissolve resist. The areas which the e-beam hit will be more susceptible to the chemical reaction and thus the desired pattern will be etched onto the surface when those parts of the photoresist layer are dissolved by the first development bath, which does not affect the lift-off resist.

The development of the lift-off resist is done to give an important effect, an undercut. The fact that the chemicals used for this development does not affect the photoresist, in combination with a longer development time than for the photoresist layer, means that some of the lift-off resist below the undissolved photoresist will be dissolved. The space thus created is called an undercut; this is illustrated in figure 4.1.

4.4 Evaporation

With the pattern in place it is time to evaporate the metals which will constitute the different structures on the chip. Before the chips are placed in the evaporator (Edwards HTPS Auto 306), they are cleaned with oxygen plasma in a vacuum chamber. This process, known as “ashing”, removes all organic materials from the surface of the chips. The chips are then placed at the top of the vacuum chamber in the evaporator, facing downwards. The evaporation layout is shown in figure 4.2.

The metals to be used for evaporation are placed in small tungsten boats, close to the chamber floor. For Al a piece of wire is placed on a quite wide boat to prevent the large drop of melted metal to fall off during evaporation. For Cr a small amount of powder is placed on a thin boat covered by a

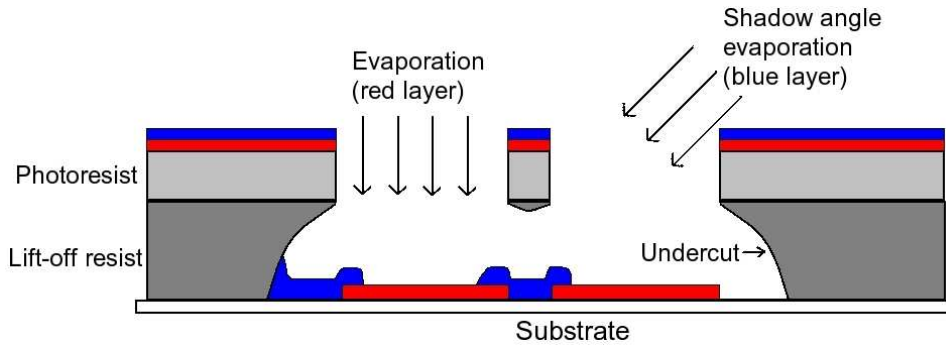


Figure 4.1: A visualization of the shadow angle evaporation technique made possible by undercut. After evaporating the first layer vertically through the gaps in the resist, the sample is tilted and the second layer reaches the space under the thin resist bridge, forming a junction. By using normal metal for the first layer, letting it oxidize to form an insulating surface and then evaporating a superconductor for the second layer we create an SIN junction. Also, the shadow angle evaporation connects the superconductor to the antenna.

ceramic tube with a small rectangular opening in the middle to simulate a point source, smaller than the Al drop.

Before evaporation, the chamber is pumped down until a pressure of $10^{-6} - 10^{-5}$ mbar is reached. This is necessary to avoid evaporating impurities onto the chip. Once the pressure is sufficiently low, the boat containing the metal to be evaporated is placed under the chips and a current is sent through it and heats it. The higher current that is sent through the boat, the quicker the metal evaporates, and the evaporation rate affects the smoothness of the surface formed. The rate of evaporation and accumulated thickness is measured by the change in resonance frequency of a crystal inside the chamber. When the metal is evaporating at a satisfactory rate, and enough metal has been evaporated for any impurities on the metal to have been evaporated already, the shutter is opened. The shutter is then closed automatically when the required amount of metal has reached the chips.

To create the junctions in the bolometer structures oxidation and a method called “shadow angle evaporation” are used. When aluminium has been evaporated on top of the chromium a small amount of oxygen can be allowed to flow into the chamber for a few minutes. This oxidizes the aluminium surface, creating the thin insulating layer in the SIN/SIS’ junctions. To complete the junctions another aluminium layer is deposited using an advanced version of “shadow angle evaporation” [33], which is shown in figure 4.1. Tilting the sample holder with the chips vis-à-vis the metal vapour flow allows us to make use of the undercut to connect previously evaporated metal layers separated by a short distance.

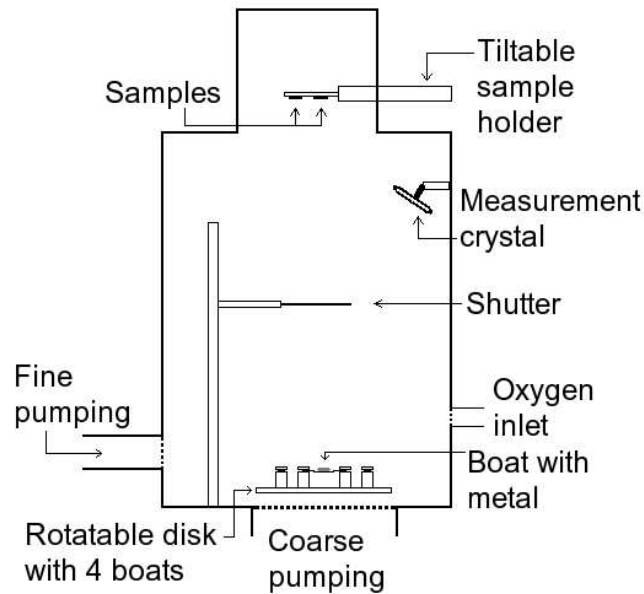


Figure 4.2: A schematic of the Edwards evaporator. When current is passed through the contacts holding the boat, the metal is heated and starts to evaporate. Opening the shutter lets the metal vapour reach the samples mounted on the tiltable sample holder. The evaporation thickness is measured by a crystal at the side of the chamber.

4.5 Lift-off

When the evaporation is done a lot of excess metal as well as resist layers, all of which are not part of the final structure, are still present on the sample. To remove them a process called lift-off is used. By applying heated chemicals ($40 - 70^{\circ}\text{C}$) called removers (e.g. acetone) we can make the lift-off resist swell and loosen its attachment to the substrate. The undercut aids this process by giving the chemicals more space under the photoresist layer to reach the lift-off resist. To aid the lift-off even more and to remove any small remains at the end of the process, ultrasound may be used, carefully, for a short time.

4.6 Optical and electronic inspections

During the manufacturing process two types of microscopes are used to inspect the bolometer chips. The optical microscope, which has the worst resolution of the two, is mainly used during fabrication to see if the development gives the proper undercut, if the lift-off is properly done and other similar checks which don't require a detailed look at the bolometer structure itself.

To see details in the bolometer structure such as the size of the tunnel junctions the SEM (Scanning electron microscope) is used on a sample where gold has been used in the evaporation of the bolometer structure. These measurements show whether or not the final e-beam exposure and development have been done optimally.

4.6.1 Optical microscope

We have used an optical microscope frequently during the fabrications to ensure that development and lift-off are properly done. By adjusting the focus back and forth, the undercut created by the development can be clearly seen and analyzed. At times when not enough undercut has been created, additional development is done and the lift-off times are prolonged. This is true also for lift-off; if the chip is not clean enough additional lift-off is used and the standard times are increased. At the same time, there is always a risk of creating too large an undercut by excessive development or affecting the evaporated structures with the lift-off.

The microscope, Olympus MX50, is connected to a computer, allowing pictures to be taken and stored. The maximum magnification of the microscope is 1000X, with maximum resolution of approximately $0.4\ \mu\text{m}$. Once the lift-off looks good, pictures of all the structures are taken. Problems like broken absorbers and junctions, scratches on the chip made by tweezers and particles that could short circuits can then be identified. One such picture is shown in figure 4.3.

4.6.2 SEM - Scanning electron microscope

For measurements requiring a higher resolution than the wavelength of visible light one option is to use an SEM (we used JSM-6301F from JEOL), which uses electrons instead of photons to create an image. The sample is loaded in a vacuum chamber, which is pumped down. Electrons are then accelerated by a high voltage, 15 kV in our case, collected into a narrow beam and focused by a system of magnetic lenses. The beam is swept across the sample by the scanning coils, which also are connected to the two monitors. When the electrons hit the sample some of them bounce off the surface; they are called backscattered electrons (BSEs). [30]

When we look at bolometer samples we use the BSEs to distinguish the structures. The strength of the signal from the BSE detector determines the brightness of the corresponding point on the monitors. The number of BSEs increases with the atomic number of the elements in the sample. For this reason gold is often used in the bolometer structures of a chip which is to be studied in the SEM, since it gives a clearer picture (see e.g. figure 3.6).

Another reason for not measuring on a real sample with junctions made of chromium and aluminium, and instead using gold which is easy to evap-

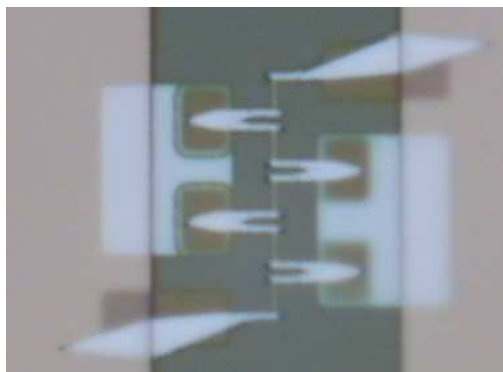


Figure 4.3: A picture of the left B2 structure on the sample L14-32, taken with the optical microscope at maximum magnification. The 5 absorbers (the thin lines in the middle, each approximately $2\ \mu\text{m}$ long) and the 10 tunnel junctions of the array structure (the connections to the absorbers) can be distinguished. All of them look as they should, the sample does not show signs of any larger errors such as broken absorbers or incomplete tunnel junctions. The absorbers are capacitively coupled to the antennas via Ti/Pd pads (the brown rectangles with a greenish edge) on oxidized aluminium (the white rectangles). A more detailed look at the tunnel junctions require the use of SEM or AFM.

orate, is that the SEM inspection slowly but surely destroys the sample. The constant bombardment of electrons would damage the fragile structures which make up the bolometer.

Chapter 5

Measurements

A great many measurements are done after the fabrication of a bolometer chip. This chapter aims to describe these measurements and the basis for the analysis of the results; it is very important in order to understand and fully comprehend the results discussed in the following chapter.

The chips that show promising characteristics at room temperature are loaded into one of the cryostats for further measurements. The samples are there cooled down to subkelvin temperatures, temperatures at which aluminium is superconducting, and IV curves for the junctions can be measured. These procedures are presented in the first part of the chapter.

The IV characteristics and their interpretations are vital for the determination of the performance of the bolometer. Hence the second and last section of this chapter describes how they are used to extract information about the quality of the bolometer.

5.1 Electronic inspections and the AFM

When the bolometer chip has been fabricated it is time for the electronic inspections. All resistances and junctions are first checked at room temperature to determine whether or not the chip's structures are working well enough to warrant more detailed investigations at cryogenic temperatures. There, finally, the resistances are checked yet again before the IV curves of the junctions are measured. Finally, if a structure shows very interesting characteristics, it may be examined more closely with AFM.

5.1.1 Room temperature checks

The room temperature measurements are done in order to check which wires, resistances and junctions seem to be working. If there are any broken connections, these may be fixed with e.g. silver paste. The sample can also be cooled with liquid nitrogen for further checks, but once a sample is deemed

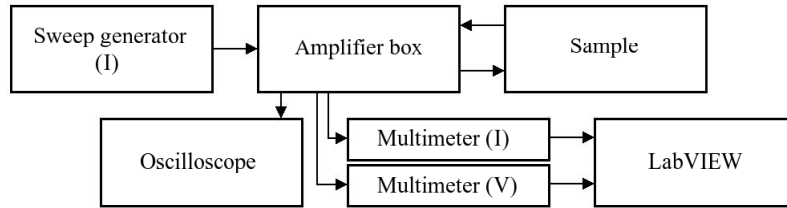


Figure 5.1: A schematic picture of the experimental setup for room temperature measurements in current bias mode.

to be interesting for IV measurements of junctions, it is cooled down to cryogenic temperatures.

For room temperature measurements a special sample holder is used as well as an amplifier box, a sweep generator, multimeters, an oscilloscope and a computer with a special LabView program. A sketch of the setup is shown in figure 5.1. The sample is placed in the sample holder, which has 16 POGO pins connecting to the contact pads on the chip. A suitable bias resistance (usually between $1\text{ M}\Omega$ and $1\text{ G}\Omega$) is chosen in the amplifier box and the sweep generator gives a current sweep. This sweep is modified after initial observations with the oscilloscope. The setup enables us to do both 2-, 3- and 4-point measurements, which are illustrated and described in figure 5.2.

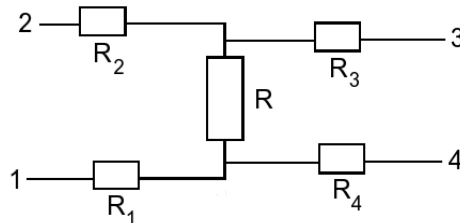


Figure 5.2: An illustration of the differences between 2-, 3- and 4-point measurements of a resistance R . The current and voltage are either measured over the same two contacts (2-point), with one contact in common (3-point) or with no contact in common (4-point). To measure R in a 2-point measurement using contacts 1 and 2 would include R_1 and R_2 in the result. A 3-point measurement, using contacts 1 and 4 to measure I and contacts 3 and 4 to measure V , would only add R_4 to the result for R . A 4-point measurement would use contacts 1 and 2 to measure I and contacts 3 and 4 to measure V ; this gives the correct value for R . 2-point measurements are used to measure all the on-chip resistors, which have resistances of approximately $150\text{ k}\Omega$ or $2\text{ M}\Omega$. 4-point measurements on the other hand are used for the junctions and the absorbers, which have resistances of a few $\text{k}\Omega$. If there is a problem with one of the contacts 3-point measurements may be used instead.

5.1.2 Cryogenics equipment and IV curves at cryogenic temperatures

For our cryogenic measurements we have used two cryostats: the HelioxTM AC-V ³He refrigerator and the TritonTM dilution refrigerator, both manufactured by Oxford Instruments. The Heliox system can reach temperatures just below 300 mK and be kept there for at least 50 hours. Triton is slightly more complicated, but can reach temperatures down to 50 mK. A measurement cycle for one of the cryostats (with vacuum pumping, cooling, measurements and heating) takes 3-4 days. For a detailed description of how the Heliox works, see appendix C.2.

To enable measurements, the sample is connected through many delicate wires to an amplifier box (just like the one used for the room temperature measurements) on top of the cryostat. At the start, the measurements are done in the same way as at room temperature: all on-chip resistors are measured in current biased mode using 2-point measurements and IV curves for the junctions are assembled using 4-point measurements. The best junctions are then selected for more detailed investigations. For each one of them we heat the sample a few hundred mK and then cool it down to base temperature again, measuring IV curves at many different temperatures on the way.

By using some additional equipment, mounted in the cryostat before it was cooled down, we can measure the response of the bolometer to radiation from an external source. This is an important experiment since it tests the entire structure, including the antennas, and not just a single junction with absorber. In figure 5.3 the setup for this is shown. Radiation is generated inside the cryo chamber by running current pulses through a sapphire substrate with a thin film of Ni and Cr on top of it. The film is heated to a temperature (not more than 40 K) inversely dependent on the frequency of the square pulses, and the modulation depth of the temperature decreases with higher frequencies. Hence, by alternating the frequency we can see how the bolometer reacts to different amounts of radiation.

5.1.3 AFM - Atomic force microscope

The AFM is used to inspect very interesting samples, with either surprisingly good or bad IV characteristics. It generates high-resolution 3D images of the tunnel junctions without damaging the structures. The smoothness of the surface and the amount of material scattered around a tunnel junction can be clearly seen, giving an indication of whether or not the optimal values for evaporation rate and thickness were used. For a detailed description of the AFM, see appendix C.1.

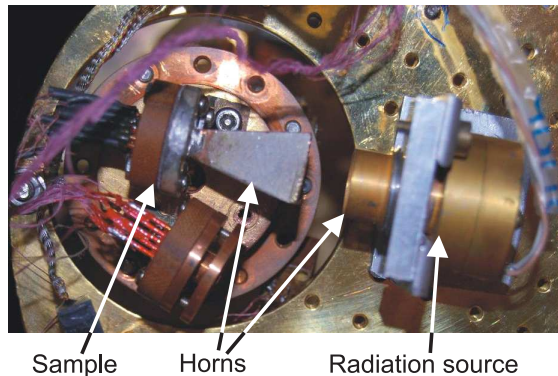


Figure 5.3: The setup for measuring the response of the bolometer to radiation. The radiation source is periodically heated and the resulting black-body radiation is focused onto the bolometer sample by two horns.

5.2 IV characteristics

The IV curves obtained in the cryogenic measurements are a valuable source of information if interpreted correctly. Below is a walkthrough of some important parameters, e.g. resistance ratio, Δ , responsivity and saturation temperature, why they are important and how they can be obtained from data. These characteristics hail from three different parts of the working structure of the CEB.

Firstly, we have the SIN junction. The better the junction is, the clearer the IV curves are. A measure of the junction quality is the resistance ratio.

Secondly, we have the absorber, where the temperature changes with incoming radiation. An important feature here is saturation.

Finally, we have the entire bolometer structure. It determines the reaction to incoming radiation: the greater the change in measured voltage due to a change in temperature in the temperature range the CEB is to measure in, the better. The relevant quantity is called responsivity; it is connected to the NEP. If the antennas and the rest of the CEB work correctly, the response to external radiation may also be analysed.

5.2.1 Resistance ratio: Subgap resistance & leakage

The quality of the tunnel junctions is determined by a wide range of factors. Among these are the thickness of the insulating layer (I) and the area of the junction. A way to quantify the quality of a junction is through the resistance ratio, defined as:

$$RR = \frac{R_S}{R_N} \quad (5.1)$$

The resistance in the subgap region, R_S , is given by the dynamic resistance $\frac{dV}{dI}$ at zero bias current. It consists of two contributions connected in par-

allel. One of the contributing resistances is unavoidable; it is due to the thermal distribution of electron energies in the absorber and comes from the tunnelling of electrons through the junction. This is very interesting, and its discoverer Ivar Giaever was awarded with a Nobel Prize in 1973. This tunnelling current makes the IV curve a bit smeared and creates a large temperature dependent resistance R_T . The other term is due to leakage, and depends only on the quality of the junction. The space between different structures on the chip may contain conducting materials scattered during the evaporation. Such small conductors around the junctions form a way for current to bypass the junction, giving rise to a leakage resistance R_l . There might also be some leakage due to the chromium layer as is described in section 3.6. The total subgap resistance hence becomes:

$$\frac{1}{R_S} = \frac{1}{R_T} + \frac{1}{R_l} \quad (5.2)$$

This means that when the temperature goes below a certain point, the leakage resistance R_l will become the dominant term, setting the upper limit of the subgap resistance. In other words the resistance ratio is a measure of how much the subgap resistance $R_S = \left. \frac{dV}{dI} \right|_{I=0}$ can change as the temperature increases, which is illustrated in figure 5.4. This is basically what we use when we measure radiation with the bolometer: the change in the IV curve given by a change of temperature.

The subgap resistance is determined from our measurements by fitting a line to the points near $I = 0$ on the IV curve and by calculating its slope, which is an approximation of $\left. \frac{dV}{dI} \right|_{I=0}$. The normal resistance R_N (see section 2.3) is extracted in a similar way, by using only the points outside the characteristic “knee”. An example of this can be found in figure 5.5.

5.2.2 The energy gap of the superconductor

Another parameter which is obtained from the IV curve of a junction is the superconductor energy gap Δ . By plotting $\frac{dI}{dV}$ we get a curve which in the best case closely resembles the DOS, see figure 5.6.

5.2.3 Saturation of absorbers

The sensitivity of the absorber to heat is one of the foremost characteristics upon which the CEB concept is built. We want our absorbers to respond heavily to incoming radiation. However, there is a conflict between large decoupling of the electron and phonon subsystems and high sensitivity of our absorbers. Incoming power can saturate the absorber, thereby setting a lower limit to the electron temperature.

Due to the cold-electron effect (see section 3.1.1), any change in incoming power will have a profound effect on the electron temperature in the

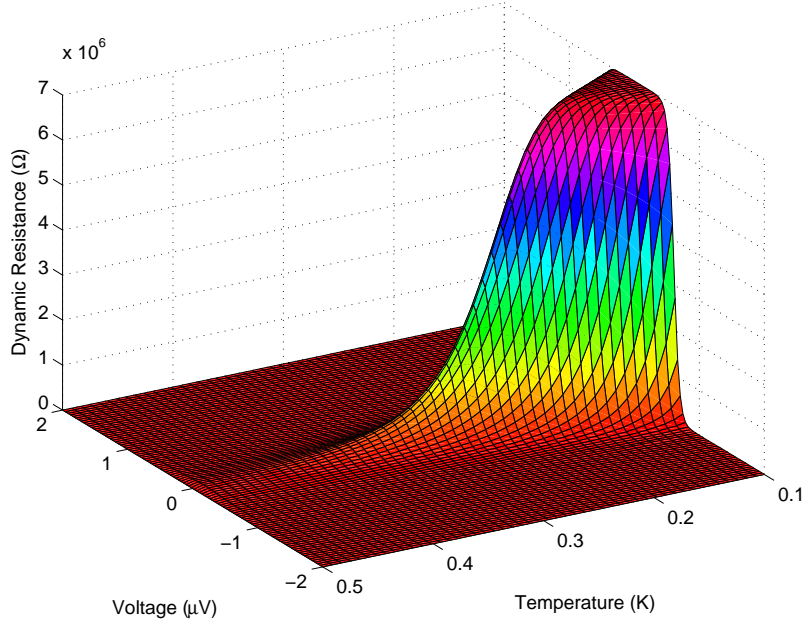


Figure 5.4: Simulated dynamic resistance as a function of the temperature and the voltage over a junction with a leakage resistance of $7 \text{ M}\Omega$. Note that the subgap resistance (the dynamic resistance at $V=0$) is essentially constant below a certain temperature where the leakage resistance dominates, while the temperature dependent resistance becomes increasingly important at higher temperatures.

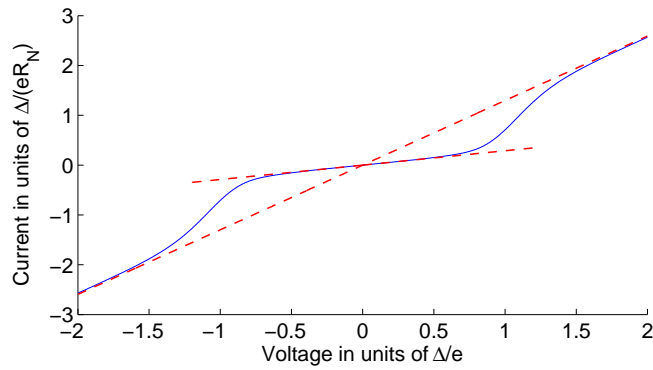


Figure 5.5: An illustration of the resistance ratio of an SIN junction. The ratio is obtained by dividing the slopes of the asymptotes. The subgap resistance is the resistance at voltages below Δ/e , while the normal resistance is the asymptotic resistance at voltages larger than Δ/e . The "knee" is where the resistance rapidly changes just above Δ/e . The slope in the subgap region is greatly exaggerated for a clearer presentation.

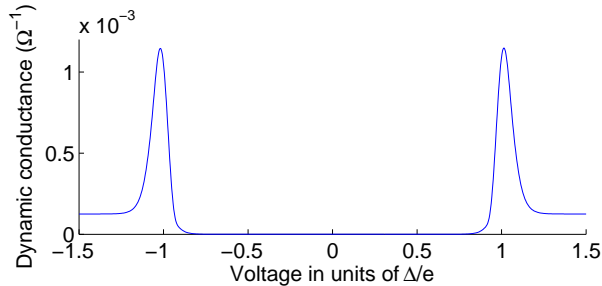


Figure 5.6: Simulated dynamic conductance ($\frac{dI}{dV}$) as a function of applied voltage over a 4 junction array at 300 mK. Note the close resemblance to the DOS presented in figure 2.2. From this plot, Δ is most easily obtained by identifying the sharp peaks in the conductance.

absorber, while not affecting the phonon temperature. Since the responsivity depends very strongly on the electron temperature, a high electron temperature means a low responsivity, as is displayed in figure 5.8.

We investigate this by analysing the voltage response of our bolometers to a change in the cryostat temperature. As long as there is a response, the electron temperature is in effect determined by the cryostat temperature. Below a certain temperature however, the heating of the absorber by the received powerload overtakes the cooling of the absorber by electron-phonon interactions and removal of hot electrons through the junction. Lowering the cryostat temperature further will then not affect the electron temperature, and the voltage response drops to zero. The absorber is then said to be saturated.

The saturation temperature can be approximated using the heat balance equation (3.8) and ignoring all terms except the external powerload. The equation then becomes:

$$\Sigma\Lambda(T_e^5 - T_{ph}^5) = \frac{P_0}{N} \quad (5.3)$$

where Λ is the volume of the absorber, P_0 is the applied powerload and N is the amount of bolometers in the array. Since the electron temperature is considerably higher than the phonon temperature in the saturated region the phonon temperature is ignored, and we can solve the equation for the electron temperature: The resulting temperature is then

$$T_{sat} = \left(\frac{P_0}{N\Sigma\Lambda} \right)^{1/5} \quad (5.4)$$

From this we see that the problem of saturation can be resolved in one of two ways: either by increasing the volume of the absorber (Λ), or by connecting several absorbers in an array (N). Increasing the absorber volume induces several undesirable effects, most notably the responsivity is

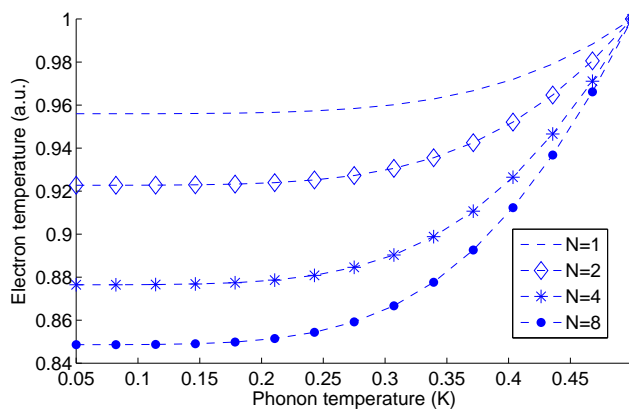


Figure 5.7: A simulation of the different saturation temperatures given by arrays of bolometers. N is the amount of bolometers in each array. The more bolometers used, the lower saturation temperature since the powerload for each bolometer is lower.

significantly reduced. An array, on the other hand, will have the effect that the power is divided between several absorbers, while still utilizing all positive effects of a small absorber volume. The effect on the saturation by connecting absorbers in an array is displayed in figure 5.7.

The saturation curves are achieved by choosing a bias current and then using the IV curves for each temperature to plot the corresponding voltage. The bias current is chosen so that we achieve minimum saturation. We have saturation when $\frac{\partial V}{\partial T} = 0$.

5.2.4 Responsivity

The responsivity of a bolometer in current bias mode, S_V , is a measure of how the bolometer reacts to a change in incoming power. With a fully working bolometer, the change in incoming power would be due to a change in the radiation that reaches the antenna. When we measure on our bolometers however, the incoming power comes from the surroundings instead. The responsivity in current biased mode is given by:

$$S_V = \left. \frac{\partial V}{\partial P} \right|_{I_{\text{bias}}} = \left. \frac{\partial V}{\partial T} \right|_{I_{\text{bias}}} \left. \frac{\partial T}{\partial P} \right|_{I_{\text{bias}}} \quad (5.5)$$

By using IV curves measured at different temperatures we can find $\frac{dV}{dT}$ as a function of temperature and bias current. $\frac{\partial P}{\partial T}$ on the other hand is just the thermal conductance of the system, which in current biased mode can be approximated by $\frac{\partial P}{\partial T} \approx G_{e-ph} + G_{cool}$, see section 3.1.1. IV curves at different temperatures are thus the key for extracting responsivity data. In figure 5.8 the simulated voltage response to a change in temperature ($\frac{dV}{dT}$) is shown

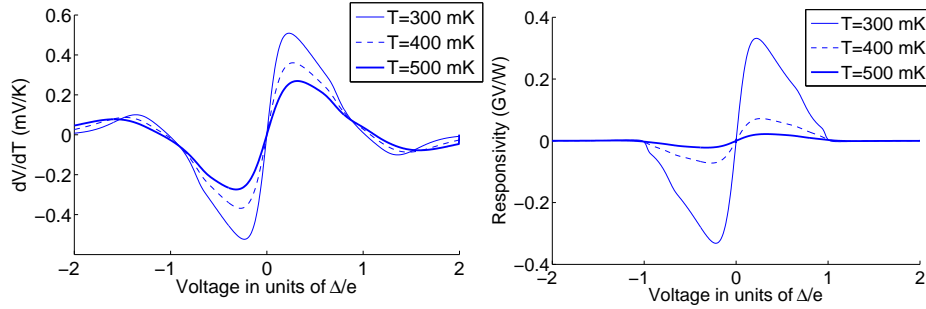


Figure 5.8: To the left: simulated voltage response to a small change in temperature at 300, 400 and 500 mK. To the right: the resulting responsivity. We very clearly see the effect of temperature on the responsivity. The parameters used for all simulations are to be found in section 3.1.1.

for a single junction, as well as the resulting responsivity. As is explained in section 3.5, the responsivity can be used to estimate the NEP of the system.

A way of measuring the responsivity directly is to heat one part of the absorber in a multiple bolometer structure (such as B5 in ARR3) and to measure the response at the other end of the absorber.

5.2.5 Response to radiation

To see the response to radiation, we use the measurements done with the Ni-Cr radiation source. Each of the IV curves produced at different heating frequencies is compared to the curve created without heating. The voltage differences are then plotted as a function of bias current (which is converted to the voltage values for the non-heated measurement), giving a picture similar to figure 5.8 with the different curves being different heating frequencies. If we observe increasing response with decreasing heating frequency, we can conclude that the bolometer is working; a lower frequency increases the modulation depth of the temperature, which should lead to an increased response.

Chapter 6

Results & Discussion

In this chapter the aim is to present our results and to put them into a context by discussion and comparison. As the goal of this project is to produce as good bolometers as possible, several parameters were changed between samples. Most notable among these are the amount of undercut, the rate of evaporation for the final structure and the oxidation time for the insulating layer of the absorber. Hence the work presented in this report cannot easily be analyzed in a quantitative manner studying the effects of changes in a single parameter. Because of this we have in most cases chosen to avoid presenting all our data but rather results from a few successful samples in this chapter. This chapter will present results that show that our bolometers have been improved significantly and are in fact near a stage where fully working samples for practical uses can be produced. The reader is encouraged to look in appendix D, where data of our twenty samples is presented.

In order to make working samples both good junctions and ditto absorbers are needed, working well together with the other parts on the chip. Therefore the results are divided into three clear sections. After a brief description of our results with making SIN and SIS' junctions we will first present the results from the manufactured junctions and an analysis of their quality. Then the properties of our absorbers are discussed to some extent. Some of our measurements include all parts of the chip; those conclude the results in this chapter. We aim to give a good understanding of our progress with the sample fabrication, but also current delimitations. Using the results we will discuss the questions: Do we have better junctions? Are our absorbers working, and have the bolometer properties been improved?

6.1 Designing absorbers for SIN and SIS'

The work with absorbers has been split into two different production lines: to make thinner normal metal absorbers for use in SIN bolometers, and to

make absorbers with thinner layers of chromium for use in SIS' bolometers. The latter requires the absorber to be a weak superconductor with a T_c near 300 mK.

In trying to decrease the absorber volume for SIN, the chromium thickness was held constant at 0.5 nm while the aluminium thickness was altered between 7, 10 & 15 nm. Keeping a thick chromium layer during the series the hope was to avoid the absorber becoming superconducting. This succeeded, and working thin absorbers have been manufactured.

In the latter line, searching for S', the combinations of 0.1, 0.2 and 0.3 nm Cr together with 10 nm Al were fabricated and so was a series with 0.2, 0.3 nm Cr with 20 nm Al. In one (L14-23ARR4) of the two 0.1 nmCr/10 nmAl samples, two SIS' junctions with T_c of 600 – 700 mK were observed. Some data to support this conclusion is shown in figure 6.1. The other sample, L10-36FIN, did not show the same behaviour for any junction, but at least one absorber showed a transition of some kind around 680 mK (The slope of the straight IV curve decreased markedly for low currents at low temperatures). In none of the other samples did the absorber show weak superconductivity characteristics in the 50 – 1000 mK region. In one sample - L14-42ARR4 - the absorbers were superconducting but with a T_c at 1.3 K, indicating that barely any chromium was evaporated onto the chip. This is regarded as a fabrication process error.

Hence, from the sample data the conclusion is drawn that chromium thicknesses down to 0.2 nm have a very strong suppressing effect on the aluminium superconductivity. At 0.1 nm the chromium did not suppress the superconductivity enough: we search for a T_c near 300 mK. This would mean that a chromium layer somewhere between 0.1 and 0.2 nm would be needed. Unfortunately, as there is a limit to the accuracy of the amount of chromium that is evaporated onto the sample it is our conclusion that weak superconducting absorbers with $T_c \approx 300$ mK cannot be made out of chromium/aluminium in a sufficiently reproducible and controlled manner using this method and the current equipment of the Bolometer Group. Due to this, the rest of this chapter will be entirely devoted to analysing SIN junctions.

6.2 Junctions

The physical phenomenon on which CEBs are based is the tunnelling of electrons across junctions. Constructing good junctions is thus a very important part of the process. In this section the aim is to present the quality of the manufactured junctions thoroughly and to conclude whether better junctions were produced or not, as well as why.

In evaluating the SIN junctions several different parameters of the IV characteristics must be studied. This section contains analyses of the resis-

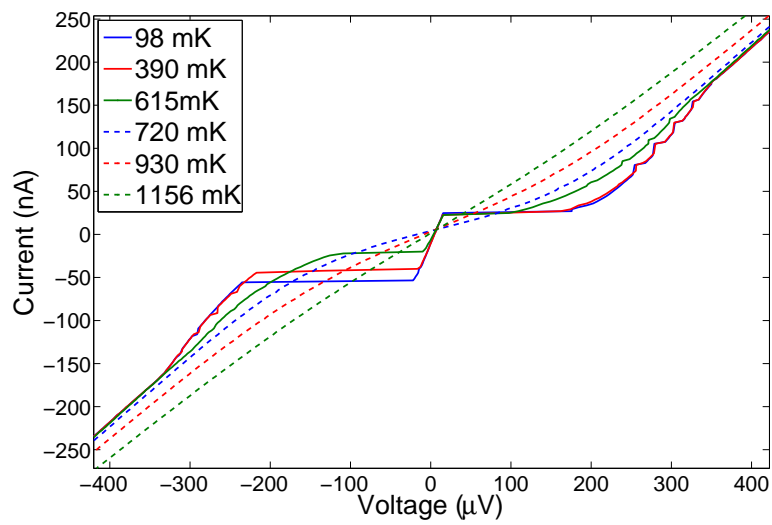


Figure 6.1: IV curves taken at different temperatures for one junction in the B3 structure on L14-23. Note the sharp transition occurring between 615 mK and 720 mK. At the lower temperatures we see a critical current typical for SIS junctions and at higher temperatures we see usual SIN characteristics, which gradually fade to a straight line when the temperature reaches 1.1 K.

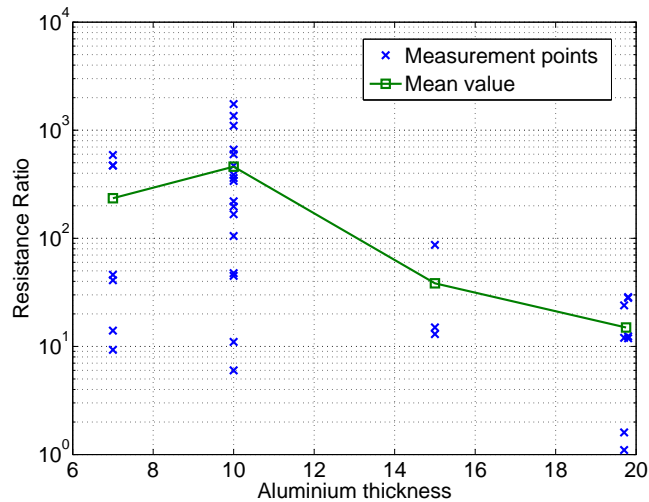


Figure 6.2: All measured resistance ratios plotted as a function of the thickness of the aluminium layer, which is the main part of the absorber volume. There is a visible trend that the resistance ratio increases with decreased absorber thickness. However, this trend should be regarded with caution since other parameters except the absorber thicknesses differ between the represented CEB structures.

tance ratio, the subgap resistance and the dynamic conductance. IV measurements have been made on promising samples at temperatures between 50 mK and 700 mK, and we will see that our best junctions correspond well with standard theoretical models at low temperatures.

6.2.1 Resistance ratio

While studying the resistance ratio RR , previously discussed in section 5.2.1, a trend of the RR s dependence on the absorber thickness has been observed; the RR seems to be improved with thinner absorbers.

Quantitative RR result The resistance ratios of all junctions with measured IV characteristics, plotted as a function of the thickness of the absorber in figure 6.2, show large deviations in quality. Still, there is a clear trend that the RR increase with decreased absorber thickness. The trend should be taken with some caution though. Resistance ratios are only available from samples that have been measured on in the cryostat, i.e. samples that worked well in the first place. Furthermore there is additional information not represented in the graph. As the thinner samples were done using a slightly altered fabrication method with a somewhat thicker insulator layer of the junctions, the possibility that these alterations are entirely responsible for the improved characteristics cannot be excluded.

The highest RR was achieved for the L10-63 sample with a 0.5 nm Cr/10 nm Al absorber. It is estimated to be above 1700, which is near the theoretical limit for our junctions. It can be compared to the Bolometer Group's previous best published result of 3200 [28] or unpublished 28000 for a previous fabrication technique. Those results were achieved with another type of bolometer made for temperature measurements. In other words we have managed to reach about the same quality of our junctions as previously but with a new fabrication process allowing, for instance, thinner absorbers.

RR differences on the same samples Apart from large deviations in RR between chips, differences have also been documented for different structures on the same chip. In those cases the normal resistance R_N is about the same while the subgap resistance R_s is varying; hence we will focus on the subgap resistance which is more important physically. The best example of a systematic difference is between the primary structures (B1/B2) and the secondary structures (B3/B4) on the ARR chips, with the primary ones having a larger R_s than the secondary ones. A typical example from an ARR3 chip is listed in table 6.1. These deviations are of a great importance to our analysis of junctions since they can help us determine what might give rise to higher resistance ratios. The important differences between the primary and the secondary structures can be divided into three categories: size, number of junctions and degree of protection from electrical interferences.

The main structural difference lies in the size of the junctions. In the two primary structures half of the junctions have a width of $0.2\ \mu\text{m}$ and $0.4\ \mu\text{m}$ respectively, while all junctions in the secondary structures have a width of $0.4\ \mu\text{m}$. It is possible that wider junctions could lead to a thinner and less homogeneous insulating layer as a result of the development and evaporation processes. This could reduce the quality of the wider junction.

Another explanation to the lower subgap resistance is saturation. As is explained in section 5.2.3, saturation of a structure will occur when the powerload P_0 from the surroundings becomes too large. The saturation is temperature dependent, and it might be that the R_s measurements were done at a temperature below the saturation temperature. Having the primary structures saturated at a lower temperature as a result of their larger number of absorbers, with larger volumes as well, would explain their consistently better characteristics; their R_s would then be higher. Hold in mind that while the primary structures consist of 4 absorbers (8 junctions) the secondary only consist of 2, with the effect that the same powerload P_0 affects the individual absorbers in the primary structures only about half as much as it affects the ones in the secondary structures.

Another difference between the primary and secondary structures is that the primary structures are shielded by external resistances, as can be seen in figure B.4 in the appendix. Shielding resistances would absorb much of the

Table 6.1: Data for different bolometer structures on L10-63 ARR3. The absorber is made of 0.5 nm Cr and 10 nm Al. Notice the different resistance ratios (RR) for the different structures. Almost without exception the RR is higher on the B1/B2 structures than on the B3/B4 structures on all manufactured ARR3 samples.

Structure	R_N	R_S	RR	$T_{\text{meas.}}$	A_{junction}	V_{absorber}	# junc.
B1	3.9 k Ω	6.8 M Ω	1747	70 mK	0.03 μm^2	0.0126 μm^3	8
B2	5.0 k Ω	3.1 M Ω	624	100 mK	0.03 μm^2	0.0126 μm^3	8
B3	4.6 k Ω	502 k Ω	37	100 mK	0.04 μm^2	0.0137 μm^3	4
B4	4.7 k Ω	330 k Ω	106	100 mK	0.04 μm^2	0.0137 μm^3	4

powerload from disturbances, leading to a lower saturation temperature of the structure. The last possibility that could explain the differences is that the absorbers have been partly burnt out. That this would have happened for all structures of the same kind seems improbable, but it is not impossible.

Unfortunately there is not enough data from the samples for us to be able to conclude what effect has caused the differences between the subgap resistances. Saturation curves for the different structures would tell whether or not there is a difference in saturation temperature between the primary and secondary structures. If the differences simply were due to the number of absorbers, the T_{sat} of the primary structures would be lower than half of that of the secondary structures. Other differences in saturation temperature could be explained by the shielding resistances. Checking for burnt-out structures could be done using AFM.

6.2.2 Change of subgap resistance with temperature

The subgap resistance is due to both leakage and a temperature dependent resistance stemming from physical properties; these were mentioned in section 5.2.1. With no leakage, the subgap resistance would approach infinity as the temperature approaches zero. However, as there is always some leakage the question is rather at what temperature, than if, the leakage resistance becomes the dominant term in the subgap resistance. For good junctions the leakage contribution is very small, and thus it becomes dominating only at very low temperatures. In our bolometers we strive for little leakage to be able to reach higher subgap resistance. Hence the change of subgap resistance as temperature changes is a good measure of the junction quality: the greater the change and the longer, the better. Study figure 6.3 for a comparison between two samples and note the drastic change in the subgap resistance between 200-300 mK for the low-leakage L10-63 B1 structure to the left, compared to that of the L10-34 T1 which show clear signs of leakage. The flatness of the top of the latter gives the leakage. The leakage

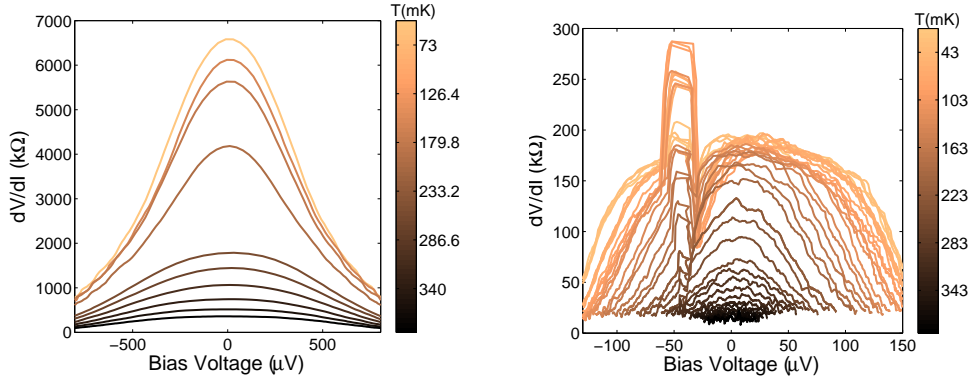


Figure 6.3: Dynamic resistance $\frac{dV}{dI}$ versus temperature and voltage over a junction for a sample with small and large leakage, respectively. The subgap resistance is the resistance near $V = 0$. To the left is the L10-63 B1 structure, showing only small signs of leakage. Note how the dynamic resistance continues to increase, although more slowly, all the way down to 50 mK. To the right is the L10-34 T1 structure, showing clear signs of leakage already at 200 mK when the subgap resistance approaches its upper limit. This has a flattening effect of the curves. There is a comparatively small temperature dependence of the dynamic resistance: the drastic change takes place between 200 and 300 mK for both structures. The reason for this is the materials used for the junctions, chosen for exactly this feature since these are the operating temperatures sought for, where the CEB should respond the most to changes in temperature.

resistance R_l can be estimated to be approximately 200 k Ω . That the left figure does not flatten even at 73 mK is a sign of a good junction with low leakage. Compare with the theoretical predictions in figure 5.4.

6.2.3 Dynamic conductance

A clear way of determining the quality of a junction is to look at the dynamic conductance $\frac{dI}{dV}$. While the resistance ratio describes the quality of a junction in the subgap region, the dynamic conductance gives information about the junction at voltages near Δ/e . For a perfect junction (that is, no leakage) at 0 K the $\frac{dI}{dV}$ characteristics is identical to the density of states of the superconductor. However, as temperature rises the DOS remains the same although the $\frac{dI}{dV}$ curve smears out some. There is a clear difference between good and bad junctions in this respect: good junctions correspond well with the DOS while bad junctions do not. A good example is figure 6.4, where the experimental results correspond well with the simulated $\frac{dI}{dV}$ curves, showing that we have nice, clean junctions with good characteristics.

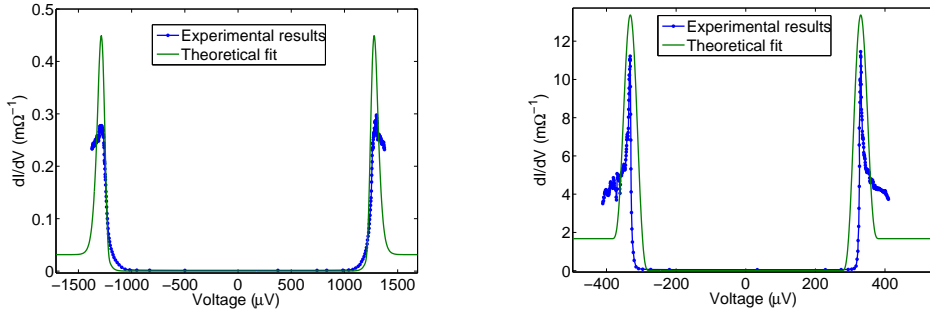


Figure 6.4: The two figures above show $\frac{dI}{dV}|_T$ for L1063ARR/B1 (left) and L933BOOM/B5 (right) together with theoretical predictions. These have been simulated with each corresponding Δ , compare with figure 5.6. Note the clear resemblance of the curves, it shows that our junctions are of a high quality. The smearing of the experimental results is due to the nonzero temperature.

6.2.4 Conclusion

Having studied the characteristics of our junctions we can conclude that we have managed to manufacture several working junctions with improved characteristics. The high resistance ratios achieved indicate junctions of significantly better characteristics than previously, able to respond more to temperature changes. Through detailed studies of the subgap resistance for some of our samples it is clear that we have managed to produce samples with virtually no leakage - a significant strength. The dynamic conductance can further validate our arguments that the quality of the produced junctions have been moved a step further towards the theoretical models. This comparison has been important for us since it is an easy way to show that the fabrication method works and produces the kind of junctions wanted.

The junctions with the best characteristics come from several different samples with different layouts. That not only one, but several, successful samples have been fabricated (see table D.2) is very important, meaning that not only have improved results been achieved, but also will the Bolometer Group be able to produce more of the same quality. Having compared different structures on the same chip we have seen that systematic difference occur there as well. These differences should be further studied with the aim of reaching a deeper understanding of the parameters affecting the quality of the bolometer junctions.

Furthermore, it has been noted that the resistance ratio seems to increase with decreasing absorber thickness. Being an important result, it is however hard to determine whether the cause of the increase in RR comes from the thinner absorbers or from other parameters of importance - such as the

thickness of the insulating layer. There is, however, a probable reason as to why a decreased absorber thickness would lead to better junctions with less leakage. This will be discussed in the latter part of the following section focusing on the absorbers.

6.3 Absorbers

Designing optimized absorbers is a crucial part of the Bolometer Group's current work and the aim of this thesis. All absorbers have been manufactured with a thin layer of chromium at the bottom and a thicker layer of aluminium at the top. The thickness of the chromium layer has been altered from 0.1 to 0.5 nm and the thickness of the aluminium layer between 7 and 20 nm on the different samples. The aim has been to decrease the volume of the absorbers. However, measuring the effect of the absorber volume alone has proven difficult. We cannot measure it without also measuring other parts of the structure, such as tunnel junctions. There is however a way to compare absorbers: to see when they are saturated. This is the focus of this section. We will see that the saturation depends on the total volume of the absorbers in a structure, as well as the number of absorbers. Our arrays work and the results seem to agree with our predictions in 5.2.3.

The decrease of the absorber thickness might also have had the unexpected consequence that the leakage around the junctions have decreased due to less scattered materials during the evaporation. This is discussed and explained in the latter part of the chapter.

6.3.1 Saturation

The saturation of an absorber is a measure of how large a powerload the absorber can cope with, as is explained in section 5.2.3. In figure 6.5 measurement series on the IV characteristics of two different structures from the same sample is shown, with temperatures in the range of 40-350 mK. From these we can see a distinct figure of importance. We note that the FIN-line structure is saturated at low temperatures. We see this because there are several curves at different temperatures very close to each other. This means that there is little change between the characteristics of the CEB at lower temperatures. This is not, to the same extent, the case with the heat sink T1 structure, which implies that the heat sink works. Hot electrons are removed through the normal metal so that the absorber is cooled down.

6.3.2 Saturation curves

The best way to study and compare saturation between structures is with the study of saturation curves. These show the voltage at a certain bias current for the sample at several different temperatures. For comparison,

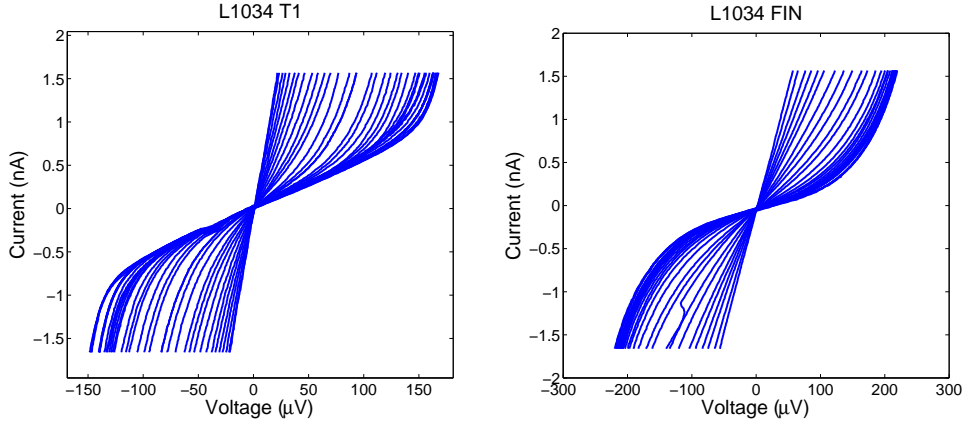


Figure 6.5: IV characteristics for two different structures from the L10-34 sample at temperatures ranging from 40 to 350 mK. To the left the heat sunk T1 structure doesn't get saturated but shows a high leakage. The latter is visible as an asymptotic line with the lowest possible tilt of $I(V)$ for the low temperature curves. To the right is the FIN structure, which has low leakage. It can be seen that the FIN structure is saturated as the low temperature curves are nearly identical to each other.

normalized saturation curves for three different structures are plotted in figure 6.6. As was explained in section 5.2.3 the saturation temperature depends on the incoming powerload P_0 to the bolometer structure, the volume of the absorber Λ and the number of absorbers connected in the array according to (5.4):

$$T_{sat} = \left(\frac{P_0}{N\Sigma\Lambda} \right)^{1/5} \quad (6.1)$$

This result makes it possible for us to diagnose our absorbers by comparing the saturation temperature of different structures.

For example, the absorber belonging to the T1 structure is heat sunk, meaning that it has a much larger volume than our normal absorbers. This is achieved by shortcutting one of the junctions connected to the absorber, making the absorber in direct contact with the antenna. We do not expect it to become saturated at all, which seems to correspond very well with our results.

The absorber belonging to the FINline structure presented in this graph is from the same sample as that of the heat sunk T1 structure. This means that there should be no differences coming from altered fabrication parameters. The FINline structure is, as can be seen in the figure, saturated at a rather large temperature. The saturation occurs at approximately 210 mK.

The B1 structure on the L10-63 sample is a 4 bolometer array, as opposed to the FINline structure which consists of only one absorber. This

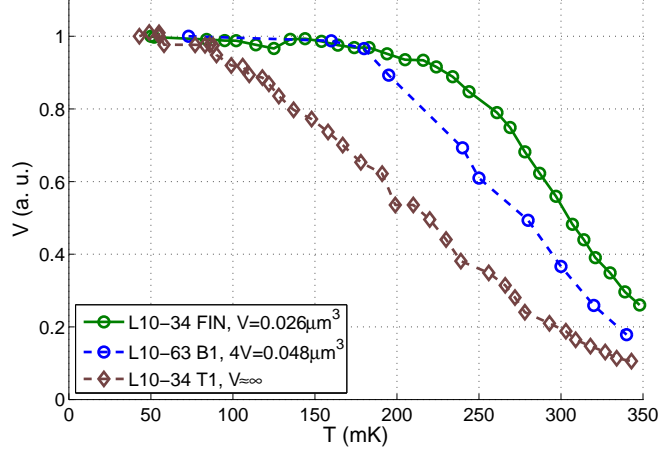


Figure 6.6: Normalized saturation curves for different structures on different samples. It can be seen that they are saturated at different temperatures, i.e. the highest temperatures where the VT curves are flat. Note the dependence of T_{sat} on the absorber volume. The T1 sample is heat sunk and should not be saturated at all, which seems to correspond well with the result.

gives us the opportunity to analyse the effect on saturation temperature of connecting several absorbers in an array. Using (6.1) and the obtained saturation temperature of the FINline structure, we find that the saturation temperature of the B1 structure should be

$$T_{sat}^{B1} = \left(\frac{\Lambda_{FIN} N_{FIN}}{\Lambda_{B1} N_{B1}} \right)^{1/5} T_{sat}^{FIN} \approx 185 \text{ mK} \quad (6.2)$$

This temperature is very consistent with our results, showing saturation of the B1 structure at about 180 mK.

From this we can conclude that we have achieved the predicted division of powerload in a series array of CEBs. Furthermore, the effect of volume on the saturation temperature is clearly demonstrated by the lack of saturation in the heat sunk T1 structure.

6.3.3 Potential decrease of leakage due to thinner absorbers

The evaporation of structures on a chip is not a very clean process on the atomic scale. Not all of the metal is deposited in the correct place; some of it is scattered near the main structures. This gives rise to leakage in the junction. In order to study the effect of the evaporation some structures are studied using the AFM. Figure 6.7 shows an AFM picture of one of the junctions in the L10-63 B1 structure. Despite the fact that this structure showed low leakage the scattered material around the absorber and the junction is clearly visible. Even so this picture, along with similar results from

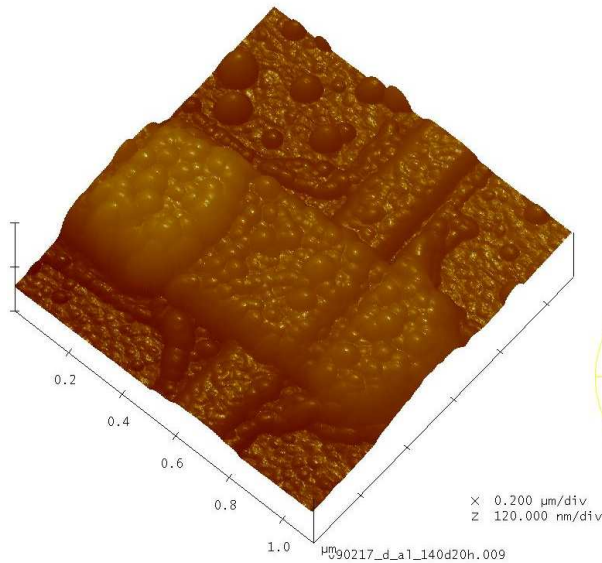


Figure 6.7: An AFM picture of one of the junctions belonging to the B1 structure on the L10-63 sample. The thin line going from the bottom left corner to the upper right corner is the absorber, which is about 15 – 20 nm thick and 200 nm wide. The larger structure is the superconducting contact with the rest of the circuit and between the two is the insulating layer (I) of the SIN junction. Take note of all the impurities in the form of small bubbles around the absorber and the contact. These are scattered during the evaporation process and give rise to leakage, but are uncommonly smooth and small due to a slightly altered manufacturing process.

the Bolometer Group, constitutes a clear indication that thinner absorbers actually reduce the amount of scattered impurities around the structures, reducing the risk of leakage. This is a very important result which might explain why higher resistance ratios were achieved with thinner absorbers.

6.3.4 Conclusion

We can conclude that the absorbers are working in the sense that they do respond to a change in temperature. Furthermore, the saturation of the absorbers at low temperature speaks of a significant decoupling of the electron and phonon subsystems as is desired in the CEB concept. The indication that thinner absorbers might lead to less leakage and hence better junctions is a surprising but welcome result. Should this indeed be true the Bolometer Group has much to gain by keeping the absorbers thin: there seems to be no negative side effects except for a higher saturation temperature. As it is also clear that connecting more absorbers in an array distributes the powerload and decreases the saturation temperature, as predicted by the models, this does not pose a problem.

6.4 Entire Bolometers

So far, the focus of the chapter has been on the quality of the tunnel junctions, and the sensitivity of our absorbers. However, all this is just indirect implications on the quality of the entire bolometer. The most direct way of determining to what extent a bolometer responds to incoming radiation is to radiate it, and measure the response. The results of such measurements are presented in this section, together with an estimated responsivity using the results from previous sections. Using this information, another important parameter is estimated, namely the noise of the system. The aim of this section is to show that our bolometers are working, and that the concept is in principle ready for real applications.

6.4.1 Response to external radiation

The measure of the bolometer's ability to respond to external radiation is called responsivity (S_V); it is in current biased mode given by $S_V = \frac{dV}{dP} = \frac{dV}{dT} \frac{dT}{dP}$ where $\frac{dT}{dP}$ is the inverse thermal conductance of the system. Hence it can be rewritten as:

$$S_V \approx \frac{1}{G_{e-ph} + G_{Cool}} \frac{dV}{dT} \quad (6.3)$$

The thermal conductances are most easily extracted numerically using the heat balance equation (3.8). A comparison with experimental results by Agulo [25] on Cold-Electron Bolometers confirms this approach. Taking the IV characteristics at varying temperatures, the response in voltage due to a change in external temperature at a constant current ($\left. \frac{dV}{dT} \right|_{I_{bias}}$) can be extracted. Three such dVdT curves for the L10-63 B1 structure are shown in figure 6.8. Using the obtained dVdT-characteristics together with the measured normal resistance of $R_N = 4 \text{ k}\Omega$, subgap resistance $R_s = 6.8 \text{ M}\Omega$, $\Delta = 1300 \text{ }\mu\text{eV}$ for an 8 junction array and an absorber volume of $0.012 \text{ }\mu\text{m}^3$, the resulting responsivity is plotted in figure 6.9. The responsivity has its maximum at a bias current of approximately 1.75 nA , corresponding to a voltage of $\frac{\Delta}{2e}$.

Using a radiation source, we have also measured the direct radiation response. The results are shown in figure 6.10. In the figure we see that increasing the frequency of the modulating current - thereby increasing the temperature of the source - yields a higher voltage response from the bolometer. We also note that the maximum response is at approximately $\frac{\Delta}{2e}$. The similarity between the direct response in this figure and the approximated response in figure 6.9 are striking. What the direct response shows, though, is that not only are the junctions and the absorber working, but so are the antennas.

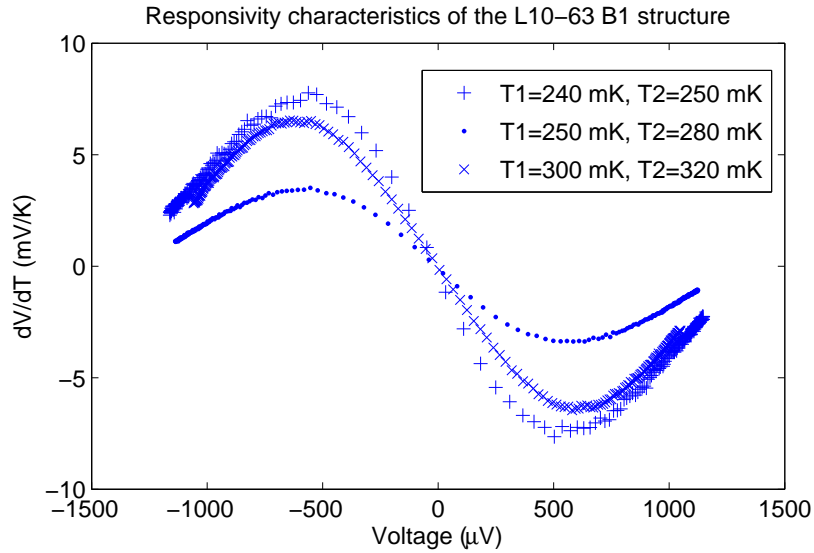


Figure 6.8: The response in voltage due to external radiation is a measure of the bolometer's efficiency. Here the $\frac{dV}{dT}$ for the L10-63 B1 structure is plotted as a function of voltage for temperatures near the CEB's working temperature at around 300 mK, compare with figure 6.5. The resulting responsivity is shown in figure 6.9.

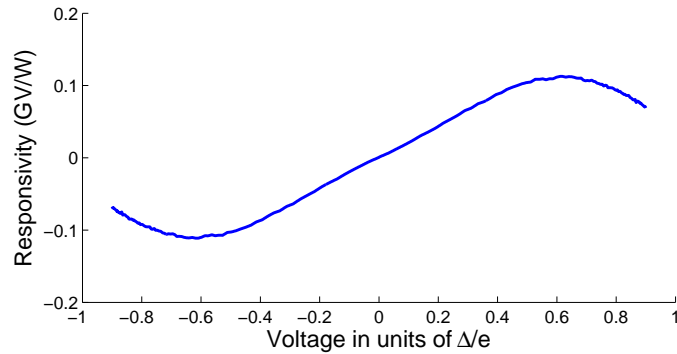


Figure 6.9: Responsivity plotted against voltage for the L10-63 B1 structure at 300 mK. The maximum responsivity is reached around $V = \frac{\Delta}{2e}$. Note the similarity between this result and the result from the direct response measurement shown in figure 6.10.

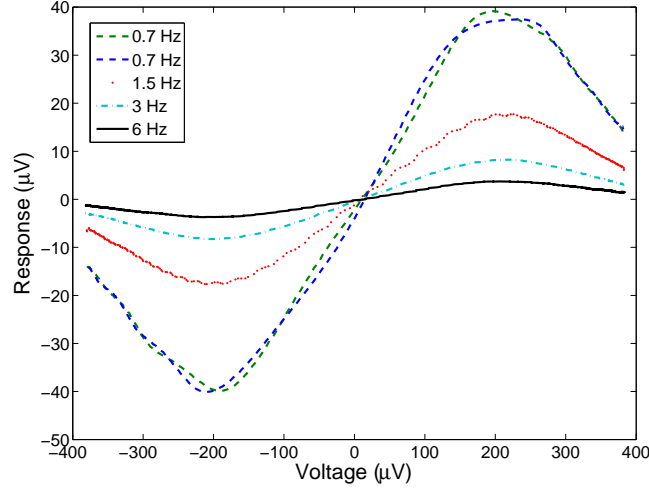


Figure 6.10: Radiation response for the structure L10-55 B1 at 278 mK. We see that the response increases with increasing frequency. The frequencies are directly correlated to the temperature of the source in the way that a lower frequency increases the source temperature.

6.4.2 Noise estimation

Using the obtained responsivity, a rough first estimate of the NEP can be done (see section 3.5). Assuming a powerload of 5 pW and a bolometer noise limited by the amplifier noise, the resulting bolometer noise is plotted in figure 6.11. The lowest value obtained is $\text{NEP} = 4.5 \times 10^{-17} \text{ W/Hz}^{1/2}$ at a bias current of 2.2 nA, corresponding to a voltage of approximately $0.75\Delta/e$. Amplifier noise of $3 \text{ nV}/\sqrt{\text{Hz}}$ and $10 \text{ fA}/\sqrt{\text{Hz}}$, values appropriate for JFET amplifiers, were assumed.

However, the validity of this approximation is bounded by the accuracy of our measurements and of the reliability of the equipment. The uncertainty of the NEP is:

$$(\Delta\text{NEP})^2 = \left(\frac{\partial\text{NEP}}{\partial e_{tot}}\Delta e_{tot}\right)^2 + \left(\frac{\partial\text{NEP}}{\partial S_v}\Delta S_v\right)^2 \quad (6.4)$$

We can see that the main contribution to the uncertainty comes from the temperature measurements, as the temperature in the cryochamber varies with a few mK during an IV measurement. However, this measurement uncertainty will only affect the responsivity, not the amplifier noise. For the

responsivity we have the uncertainty:

$$(\Delta S_v)^2 = \left(\frac{\partial S_v}{\partial T} \Delta T \right)^2 = \left[\left(\frac{\partial S_v}{\partial G} \frac{\partial G}{\partial T_e} \frac{\partial T_e}{\partial T} \right)^2 + \left(\frac{\partial S_v}{\partial \left(\frac{dV}{dT} \right)} \frac{\partial \left(\frac{dV}{dT} \right)}{\partial T} \right)^2 \right] (\Delta T)^2 \quad (6.5)$$

Using the saturation curves (figure 6.6) it is possible to approximate $\frac{\partial}{\partial T} \left(\frac{dV}{dT} \right)$ for the L10-63 B1 structure to approximately -0.4 mV/K^2 for 8 junctions. As for the temperature uncertainty ΔT , Agulo [25] measured the temperature stability of our cryogenics system to be $\pm 100 \mu\text{K}$. More importantly, since the temperature measurements were conducted while the temperature was changing continuously, the temperature will change slightly while taking the IV characteristics. At 300 mK we estimate that in the worst case scenario, the temperature changes 3 mK during the measurement. We thus take $\Delta T = 3 \text{ mK}$. Furthermore, we assume that the electron temperature changes in approximately the same manner as the phonon temperature, i.e. that the bolometer is not saturated. Hence we take $\frac{\partial T_e}{\partial T} \approx 1$. This is validated by the lack of saturation of the L10-63 B1 structure at 300 mK as is evident from figure 6.6.

Using the equations for the responsivity and the thermal conductance we then get an uncertainty in the NEP of $\Delta \text{NEP} \approx 0.9 \times 10^{-17} \text{ W/Hz}^{1/2}$ at 2.2 nA. Our resulting amplifier NEP is thus $\text{NEP} = (4.5 \pm 0.9) \times 10^{-17} \text{ W/Hz}^{1/2}$. We see that the amplifier NEP of the structure is basically identical to the photon noise at optimum bias. It is important to realize however, that this is a very crude approximation of the total noise in the sense that we disregard the effect of thermal and junction noise. For an exact characterisation of the total noise in our fabricated samples, more detailed measurements must be conducted.

6.4.3 Conclusion

We have, in a very direct manner, showed that our bolometers respond to external radiation. Furthermore, the NEP was in a crude approximation found to be below photon noise at a bias current of 2.2 nA and an optical powerload of 5 pW. Although the approximation is rough, we can conclude that photon limited NEP is a very reachable goal for the concept.

6.5 Main results and conclusions

We conclude this chapter with a review of our conclusions and some notes on questions that still need to be answered.

We have achieved weak superconductivity by reducing the thickness of the Cr layer in the absorber down to 0.1 nm, giving a critical temperature of 600–700 mK. However, since we have not seen weak superconductivity with

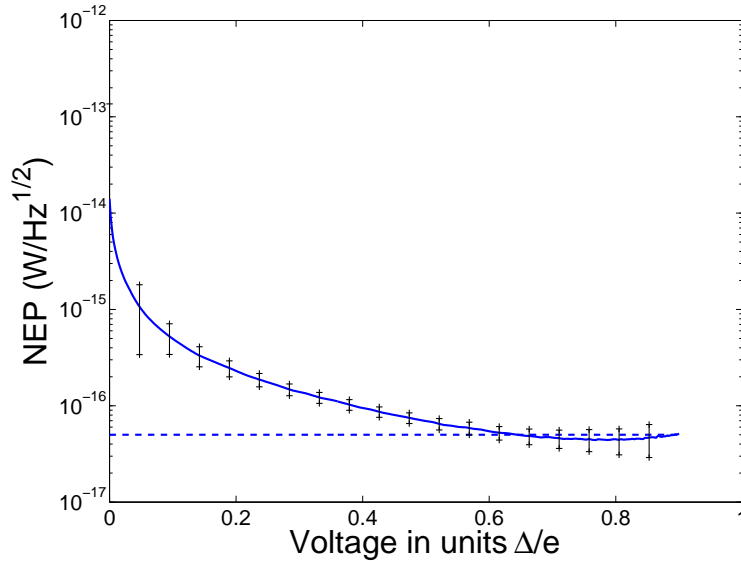


Figure 6.11: Estimated NEP based on experimental data, for an optical powerload of 5 pW, plotted as a function of voltage normalised to Δ , together with estimated uncertainties. The lowest value obtained is $\text{NEP} = (4.5 \pm 0.9) \times 10^{-17} \text{ W/Hz}^{1/2}$ at a bias current of 2.2 nA, corresponding to approximately 0.75Δ .

0.2 nm Cr, the dependence of T_c on the thickness is probably very delicate. With the currently available equipment for fabrication it will be very hard to achieve the desired critical temperature in a reproducible way using the methods presented in this thesis.

The reduction of Al thickness in the absorber, together with some small changes in fabrication parameters, has yielded bolometers with improved characteristics. We have observed increased resistance ratios and low leakage, which means the tunnel junctions are working well. The bolometers respond both to external radiation and internal changes in temperature, and are saturated at high temperatures, which means the absorbers are very sensitive. The concept of arrays enables us to retain this sensitivity while avoiding saturation at the operating temperature. Finally, an approximation of the NEP shows that the photon noise limit is well within the reach of the bolometers.

The systematic difference between the B1/B2 and B3/B4 structures needs to be explained. By measuring the saturation temperature of the structures, the powerload received to each absorber due to external interferences can be deduced. Since the B3/B4 structures consist of an array of 2 bolometers, while the B1/B2 array consists of 4 bolometers, the received powerload is expected to be twice as large on the B3/B4 chip, leading to a higher saturation temperature. However, if shielding by resistances play an

important role as well, the received powerload should be even higher for the B3/B4 structures, leading to an even higher saturation temperature.

Furthermore, it would be interesting to fabricate even thinner absorbers for an enhanced understanding of the physical premises limiting our development. We should also fabricate even more samples with absorber thicknesses from 7-20 nm for more reliable statistics. Although there is a clear trend of increasing RR with decreasing absorber thickness, the possible effect of the altered fabrication process cannot be neglected. In particular, the oxidation time, and hence the thickness of the insulating layer, was not constant during the project. By fabricating more samples, we hope to determine the effect of the insulating layer on the quality of our junctions.

Chapter 7

Summary and Future Prospects

Cold-Electron Bolometers are very sensitive devices that can be used to measure both heat and radiation. In the case of radiation, photons are led by antennas to a thin metal strip called the absorber. The absorber is either made of a normal metal or a weak superconductor; it is a critical part of the CEB. Separated from the absorber by a thin insulating layer are two superconducting contacts. The photons excite electrons in the absorber, causing them to tunnel through the SIN/SIS' junctions. An applied bias voltage/current makes it possible to convert the tunnelling to a temperature reading.

In this thesis the aim has been to improve the CEBs for use as radiation measurement devices in the BOOMERanG balloon project. The focus has been on improving the absorbers in the bolometers in two different ways: the first being to reduce the volume of the absorber for use in SIN based bolometers, as a reduced volume would mean a higher response to incoming power, and the second being to make a superconducting absorber with $T_c \approx 300$ mK for use in SIS' based bolometers. The absorbers have been fabricated with a thin bottom layer of chromium, which suppresses superconductivity of the top aluminium layer. To create the absorber for the SIS' bolometers the chromium thickness was decreased.

In the SIS' line we found that suppressing superconductivity using Cr is a delicate problem. Down to a thickness of 0.2 nm Cr there was no indication of superconductivity even at temperatures as low as 50 mK. For a thickness of 0.1 nm we observed a Josephson current, characteristic for SIS junctions, up to temperatures of 600 – 700 mK. We conclude that it is very difficult to finely tune T_c by changing Cr thickness with the existing fabrication equipment.

SIN based bolometers were successfully fabricated with much improved parameters. We have managed to manufacture absorbers with Al thick-

nesses as low as 7 nm without introducing superconductivity and retaining, even improving, relevant characteristics. The resistance ratio, a quality measure of the SIN tunnel junctions, has on several samples reached the same levels as previous efforts by the Bolometer Group some five years ago before the fabrication methods were changed. This means that we are almost back where the group was then, but with much thinner and more sensitive absorbers and larger tunnel junctions. However, the exact reason for the improved characteristics is not entirely uncovered by our work. There are two possible explanations: either the thinner absorbers have decreased the leakage in the junctions or some of the other changes made in the fabrication process have improved the junctions. A suggested way of explicitly determining the cause for this would be to produce a few more samples while varying only one of the relevant parameters.

Further advanced measurements on one of our samples were conducted using an external radiation source. Using this, we have clearly seen that our fabricated bolometers do respond to external radiation. This is exactly the desired result, and with our improved characteristics we believe that the improved CEB concept with thinner SIN junctions in array soon will be ready for space!

7.1 Future prospects

There are some supplementary measurements which should be performed to confirm our results and examine them in greater detail. These include measuring the saturation temperature of the different structures on one and the same chip to explain the systematic difference between B1/B2 and B3/B4. A more detailed study, using more samples where only one parameter is varied, of the impact a change in absorber volume has would also be of interest.

The next step in the development of fully working bolometers is to perfect the polarization measurements. So far we have only looked at single junctions or structures, but for polarization measurements four structures should be connected to make use of the cross-slot antenna or the circular waveguide discussed in section 3.7. The equipment for producing polarized radiation from the external radiation source we have used is already in place.

In a more general perspective, voltage biased bolometers are a very enticing prospect. The future development for the array structures involves the fabrication and testing of absorbers connected in parallel. For these, voltage biased mode would be the natural choice; the response from the absorbers would add up to the same response as for a single SIN/SIS' junction while the advantages of both having the powerload distributed between the absorbers and having the full cold-electron effect could be utilized. The first of these systems is a Focal Plane Array with 64 or 256 bolometers connected in

parallel. Such a system could, with good enough CEB:s, be used for better imaging of the CMBR with the hope of further deepening our knowledge and understanding of the early Universe.

Bibliography

- [1] Krane, K.S., 1988. *Introductory Nuclear Physics*, New Jersey, USA: John Wiley & Sons, Inc.
- [2] Hu, W., White, M. (2004) The cosmic symphony. *Scientific American*, February issue.
- [3] Richards, P.L. (2009). *Measurements of the Cosmic Microwave Background and the Development of Improved Detectors*, lecture, Göteborg.
- [4] Fixsen, D.J., Cheng, E.S., Gales, J.M., Mather, J.C., Shafer, R.A., Wright, E.L. (1996) The cosmic microwave background spectrum from the full COBE FIRAS data set. *Astrophysical Journal* **473**, 576.
- [5] Seife, C. (2003). Illuminating the Dark Universe, *Science*, **302**, 2038.
- [6] North, C.E. et al. (2007) *Clover - measuring the CMB B-mode polarisation*. 18th Int. symposium on Space Terahertz Technology, Pasadena, California
- [7] Kuzmin, L. *Capacitively Coupled Hot Electron Microbolometer as Perspective IR and Sub-mm Wave Sensor* Proceeding of the 9th International Symposium on Space Terahertz Technology, Pasadena, pp 99-103, March 1998.
- [8] Kuzmin, L. *Ultimate Cold-Electron Bolometer with Strong Electrothermal Feedback* Proc. of SPIE conference "Millimeters and Submillimeter Detectors", Vol. 5498, pp 349-361, Glasgow, June 21-25, 2004.
- [9] Halusa, G. (2009). *Samuel Pierpont Langley (1834-1906)* Short biography. Nasa, Earth Observatory, viewed 14 May 2009. <<http://earthobservatory.nasa.gov/Features/Langley/printall.php>>
- [10] Kuzmin, L. (2008) A Superconducting Cold-Electron Bolometer with SIS' and Josephson Tunnel Junctions. *Journal of Low Temperature Physics*, **151**, 292

- [11] Kuzmin, L. (2008) A parallel/series Array of Cold-Electron Bolometers with SIN Tunnel Junctions for Cosmology Instruments. *European Superconductivity news forum*, No.3
- [12] Kuzmin, L. (2008) Array of Cold-Electron Bolometers with SIN Tunnel Junctions for Cosmology Experiments. *Journal of Physics: Conference series* **97**
- [13] Tarasov, M., Kuzmin, L., Kaurova, N., Fiadino, P., Claudio, V., Myrin, A., Bisht, A (2009) Multilayers with Al for use in superconducting devices. *Not yet published*
- [14] Cochran, J.F., Mapother, D. E. (1958) Superconducting Transition in Aluminum. *Physical Review* 111, 132–142.
- [15] BOOMERanG - balloon telescope: Measurements of CMB Polarization, Paolo de Bernardis, Rome University, viewed 19 May 2009. <<http://oberon.roma1.infn.it/boomerang/b2k/>>
- [16] de Bernardis, P. *Plans and requirements for BOOMERanG3*, Private communication with L. Kuzmin, 2009.
- [17] Kuzmin, L. *Discussions on every aspect of CEBs*[conversation], Private communication, spring 2009.
- [18] Tarasov, M. *Discussions on every aspect of CEBs*[conversation], Private communication, spring 2009.
- [19] Kittel, C. (2005). *Introduction to Solid State Physics*. New Jersey, USA: John Wiley & Sons, Inc.
- [20] Waldram, J.R. (1996) *Superconductivity of Metals and Cuprates*. IOP publishing, London, England
- [21] Gorter, C.J., Casimir, H. (1934) On Supraconductivity I. *Physica*, Vol.1, Issue 1-6, p.306-320
- [22] Bardeen, J., Cooper, L.N., Schrieffer, J.R. (1957) Theory of Superconductivity. *Physical Review*, **108**, **5**
- [23] Olsson, K. (2008) *A Novel Concept of the Cold-Electron Bolometer with SIS' and Josephson Tunnel Junctions*. Master Thesis at the department of Microtechnology and Nanoscience (MC2), Chalmers University of Technology, Gothenburg
- [24] Wellstood, F.C., Urhina, C., Clarke, J. (1994) Hot-electron effects in metals, *Physical Review B*, **49**, **9**

- [25] Agulo, I.J.A. (2007) *Ultrasensitive Cold-Electron Bolometer*. Ph.D Thesis at the Department of Microtechnology and Nanoscience (MC2), Chalmers University of Technology, Gothenburg
- [26] Chouvaev, D. (2001), Normal metal hot-electron microbolometer, Ph.D. thesis at MC2, Chalmers University of Technology, Gothenburg
- [27] Agulo, I.J et.al (2004) Effective electron microrefrigeration by superconductor-insulator-normal metal tunnel junctions with advanced geometry of electrodes and normal metal traps, *Nanotechnology* **15** 224-228
- [28] Kuzmin, L et al (2004) Optimization of electron cooling by SIN tunnel junction *Superconductor Science and Technology* **17** 400-405
- [29] Pitaevskii, L., Stringari, S. Bose-Einstein Condensation, Oxford Science Publications, 2003
- [30] Hafner, B. (2007). *Scanning Electron Microscopy Primer*, Characterization Facility, University of Minnesota – Twin Cities, http://www.charfac.umn.edu/instruments/sem_primer.pdf [2009-05-05]
- [31] Richards, P.L. Bolometers for infrared and millimeter waves, *J. Appl. Phys.*, 76(1):1-24, July 1994
- [32] Golubev, D., Kuzmin, L., Nonequilibrium Theory of a hot-electron bolometer with normal metal-insulator-superconductor tunnel junction, *J. Appl. Phys.* 89(11):6464-6472, June 2001
- [33] Kuzmin, L. *Self-Aligned Shadow-Evaporation Technology for Large Area Tunnel Junctions and Nanoabsorbers*, US Patent, to be filed through Chalmers Industriteknik (June 2009).
- [34] *Atomic Force Microscopes*, Pacific Nanotechnology, Inc., Santa Clara, USA, viewed 5 May 2009. <<http://www.pacificnanotech.com/afm-tutorial.html>>
- [35] *HelioxTM AC-V, 300 mK Cryofree® 3He system*, Oxford Instruments, United Kingdom, viewed 5 May 2009. <<http://www.oxford-instruments.co.uk/products/low-temperature/3he-refrigerators/helioxac-v/Pages/helioxac-v.aspx>>
- [36] Delsing, P. (2009). *Lecture notes on Superconductivity and Low Temperature Physics*, Chalmers University of Technology, Göteborg, <http://mina4-49.mc2.chalmers.se/delsing/Superconductivity/Lectures.html> [2009-05-06]

Appendix A

Recipes

A.1 L9

L9 was a silicon wafer with 36 bolometers. It contained both ARR3, BOOM and FIN structures. The first layer consisted of the contact pads and the wiring, the second layer contained the resistors and the third layer was the bolometer structures.

A.1.1 Layer 1

Resist

Spin lift-off resist LOR3A at 2500 rpm for 1 min.
Bake the wafer on a hotplate at 180 °C for 5 min.
Spin photoresist UV-5 at 3000 rpm for 1 min.
Bake the wafer on a hotplate at 130 °C for 5 min.

Exposure (E-beam Lithograph JEOL JBX-5DII)

Exposure time: 2.5 h E-beam lens: 4th
Dose: 14 $\mu\text{C}/\text{cm}^2$ E-beam current: 20 nA

Postbaking

Postbake the wafer on a hotplate at 130 °C for 20 min.

Development

Put the wafer in a bath of the developer MF-24A for 1 min 30 s.
Rinse in water and blowdry with nitrogen.

Ashing (Plasma Therm Batchtop PE/RIE m/95)

Use oxygen plasma for 60 s at a power of 50 W to remove organic materials from the chip.

Evaporation (Edwards HTPS)

1. 10 nm Cr at a rate of 0.1 nm/s.
2. 130 nm Au at a rate of 0.2 nm/s.
3. 10 nm Pd at a rate of 0.2 nm/s.

Lift-off

Put in bath of Shipley 1165 Remover for 25 min at a temperature of 60–70 °C (until all Au is removed). Use ultrasound at lowest power for 3 min . Rinse in isopropanol and water, then blowdry with nitrogen.

A.1.2 Layer 2

Resist

Spin lift-off resist LOR3A at 3000 rpm for 1 min.
Bake the wafer on a hotplate at 190 °C for 5 min.
Spin photoresist UV-5 at 4000 rpm for 1 min.
Bake the wafer on a hotplate at 130 °C for 5 min.

Exposure

Exposure time: 2.5 h E-beam lens: 4th
Dose: 15 $\mu\text{C}/\text{cm}^2$ E-beam current: 3 nA

Postbaking

Postbake the wafer on a hotplate at 130 °C for 20 min.

Development

Put the wafer in a bath of the developer MF-24A for 1 min 15 s.
Rinse in water and blowdry with nitrogen.

Ashing (Plasma Therm Batchtop PE/RIE m/95)

Use oxygen plasma for 30 s at a power of 50 W to remove organic materials from the chip.

Evaporation (Edwards HTPS)

1. 12 nm Ti at a rate of 0.1 nm/s.
2. 3 nm Cr at a rate of 0.1 nm/s.

Lift-off

Put in bath of Shipley 1165 Remover for half an hour (or until all thin gold is removed) at a temperature of 60 – 70 °C. Use ultrasound at lowest power for 3 min. Rinse in isopropanol and water, then blowdry with nitrogen.

A.1.3 Layer 3

Resist

Spin MMA(8.5) MAA EL10 at 5000 rpm for 1 min.
Bake the wafer on a hotplate at 170 °C for 5 min.
Spin PMMA A4 at 6000 rpm for 1 min 40 s.
Bake the wafer on a hotplate at 160 °C for 5 min.

Exposure

E-beam lens: 5th Dose: 300 $\mu\text{C}/\text{cm}^2$ E-beam current: 80 pA

Development

See individual chips.

Ashing (Plasma Therm Batchtop PE/RIE m/95)

Use oxygen plasma for 30 s at a power of 50 W to remove organic materials from the chip.

Evaporation (Edwards HTPS)

See individual chips.

Lift-off

See individual chips.

A.2 L10

L10 was an oxidized silicon wafer with 36 bolometers. It contained both ARR3, BOOM and FIN structures. The first layer consisted of the contact pads and the wiring, the second layer contained the resistors and the third layer was the bolometer structures.

A.2.1 Layer 1

The same as for L9 with the following exceptions:

Exposure (E-beam Lithograph JEOL JBX-5DII)

Exposure time: 5.5 h E-beam lens: 4th
Dose: 14 $\mu\text{C}/\text{cm}^2$ E-beam current: 10 nA

Lift-off

Put in bath of Shipley 1165 Remover for 20 min (or until all Au is removed) at a temperature of 40 °C. Use ultrasound at lowest power. Rinse in isopropanol and water, then blowdry with nitrogen.

A.2.2 Layer 2

The same as for L9 with the following exception:

Lift-off

Put in bath of Shipley 1165 Remover for 72 h (or until all thin gold is removed) at a temperature of 71 °C. Use ultrasound at lowest power for 2 min. Rinse in isopropanol and water, then blowdry with nitrogen.

A.2.3 Layer 3

The same procedure as L9 for Resist, Exposure and Ashing. For Development, Evaporation and Lift-off, see individual chips. The data for L10-63ARR3 is shown below.

Development

1. Bathe in toluene:isopropanol = 1:3 for 50 s. Stop in isopropanol.
2. Bathe in ECA:ethanol = 1:5 for 10 min. Stop in Isopropanol .

Evaporation (Edwards HTPS)

See table A.1.

Lift-off

Put in bath of acetone for 1 h at a temperature of 40 °C. Rinse in isopropanol and water, then blowdry with nitrogen.

A.3 L14

L14 was a silicon wafer with 36 bolometers. It contained only ARR4. The first layer consisted of the contact pads and the wiring, the second layer contained Al strips to form capacitances and the third layer was the resistors

Table A.1: The parameters used during evaporation for L10-63ARR3.

Material	Cr	Al	O ₂	Al
Angle	0°	0°		45°
Type of boat	Narrow, w/ tube	Wide		Wide
Type of material	Powder	Wire		Wire
Pre-evaporation thickness [nm]	2.4	21.3		22.3
Evaporation rate [nm/s]	0.1	0.4-0.5		0.4-0.7
Thickness [nm]	0.5	10		92
Base pressure [mbar]	$1.6 \cdot 10^{-6}$	$1.5 \cdot 10^{-6}$		$1.8 \cdot 10^{-6}$
Process pressure [mbar]	$5.5 \cdot 10^{-5}$	$1 \cdot 10^{-5}$	$7 \cdot 10^{-2}$	$6.5 \cdot 10^{-6}$
Current	33	43		43-47
Cooling time/oxidization time	5 min/	5 min/	/7 min	5 min/

and the completion of the capacitances. Finally, the fourth layer contained the bolometer structures.

A.3.1 Layer 1

Resist

Spin lift-off resist LOR3A at 2500 rpm for 1 min.
 Bake the wafer on a hotplate at 180 °C for 5 min.
 Spin photoresist UV-5 at 3000 rpm for 1 min.
 Bake the wafer on a hotplate at 130 °C for 2 min.

Exposure (E-beam Lithograph JEOL JBX-5DII)

Exposure time: 3.5 h E-beam lens: 4th
 Dose: $14 \mu\text{C}/\text{cm}^2$ E-beam current: 20 nA

Postbaking

Postbake the wafer in an oven at 130 °C for 12 min.

Development

Put the wafer in a bath of the developer MF-24A for 1 min 25 s.
 Rinse in water and blowdry with nitrogen.

Ashing (Plasma Therm Batchtop PE/RIE m/95)

Use oxygen plasma for 30 s at a power of 50 W to remove organic materials from the chip.

Evaporation (Edwards HTPS)

1. 10 nm Cr at a rate of 0.1 nm/s.
2. 150 nm Au at a rate of 0.2 nm/s.
3. 10 nm Pd at a rate of 0.2 nm/s.

Lift-off

Put in bath of Shipley 1165 Remover for 20 min at a temperature of 60 – 70 °C (until all Au is removed). Use ultrasound at lowest power. Rinse in isopropanol and water, then blowdry with nitrogen.

A.3.2 Layer 2

Resist

Spin lift-off resist LOR3A at 3000 rpm for 1 min.
Bake the wafer on a hotplate at 180 °C for 10 min.
Spin photoresist UV-5 at 3000 rpm for 1 min.
Bake the wafer on a hotplate at 130 °C for 2 min.

Exposure (E-beam Lithograph JEOL JBX-5DII)

Exposure time: 3 min E-beam lens: 4th
Dose: 14 $\mu\text{C}/\text{cm}^2$ E-beam current: 10 nA

Postbaking

Postbake the wafer in an oven at 130 °C for 15 min.

Development

Put the wafer in a bath of the developer MF-24A for 1 min 30 s.
Rinse in water and blowdry with nitrogen.

Ashing (Plasma Therm Batchtop PE/RIE m/95)

Use oxygen plasma for 30 s at a power of 50 W to remove organic materials from the chip.

Evaporation (Edwards HTPS)

20 nm Al at a rate of 0.3 nm/s.

Lift-off

Put in bath of Shipley 1165 Remover for 45 min at a temperature of 70 °C (until all Al is removed). Use ultrasound at lowest power. Rinse in isopropanol and water, then blowdry with nitrogen.

A.3.3 Layer 3

Resist

Spin lift-off resist LOR3A at 3000 rpm for 1 min.
Bake the wafer on a hotplate at 175 – 180 °C for 5 min.
Spin photoresist UV-5 at 4000 rpm for 1 min.
Bake the wafer on a hotplate at 130 °C for 5 min.

Exposure (E-beam Lithograph JEOL JBX-5DII)

Exposure time: 1 h 15 min E-beam lens: 4th
Dose: 15 $\mu\text{C}/\text{cm}^2$ E-beam current: 3 nA

Postbaking

Postbake the wafer in an oven at 130 °C for 20 min.

Development

Put the wafer in a bath of the developer MF-24A for 1 min 30 s.
Rinse in water and blowdry with nitrogen.

Ashing (Plasma Therm Batchtop PE/RIE m/95)

Use oxygen plasma for 30 s at a power of 50 W to remove organic materials from the chip.

Evaporation (Edwards HTPS)

1. 12 nm Ti at a rate of 0.1 nm/s.
2. 3 nm Pd at a rate of 0.1 nm/s.

Lift-off

Put in bath of Shipley 1165 Remover for half an hour at a temperature of 70 °C (until all Au is removed). Use ultrasound at lowest power for 2 min .
Rinse in isopropanol and water, then blowdry with nitrogen.

A.3.4 Layer 4

Ashing (Plasma Therm Batchtop PE/RIE m/95)

Use oxygen plasma for 15 s at a power of 50 W to remove organic materials from the chip.

Resist

Spin MMA(8.5) MAA EL10 at 3000 rpm for 1 min.

Bake the wafer on a hotplate at 160 °C for 5 min.

Spin PMMA A4 at 6000 rpm for 1 min.

Bake the wafer on a hotplate at 150 °C for 2 min.

Exposure (E-beam Lithograph JEOL JBX-5DII)

Exposure time: 45 min E-beam lens: 5th

Dose: 300 $\mu\text{C}/\text{cm}^2$ E-beam current: 80 pA

Development

See individual chips.

Ashing (Plasma Therm Batchtop PE/RIE m/95)

Use oxygen plasma for 30 s at a power of 50 W to remove organic materials from the chip.

Evaporation (Edwards HTPS)

See individual chips.

Lift-off

See individual chips.

Appendix B

Layouts

The figures B.1 to B.8 below show the CAD layouts and the simplified layouts for BOOM6, ARR3, ARR4 and FIN4.

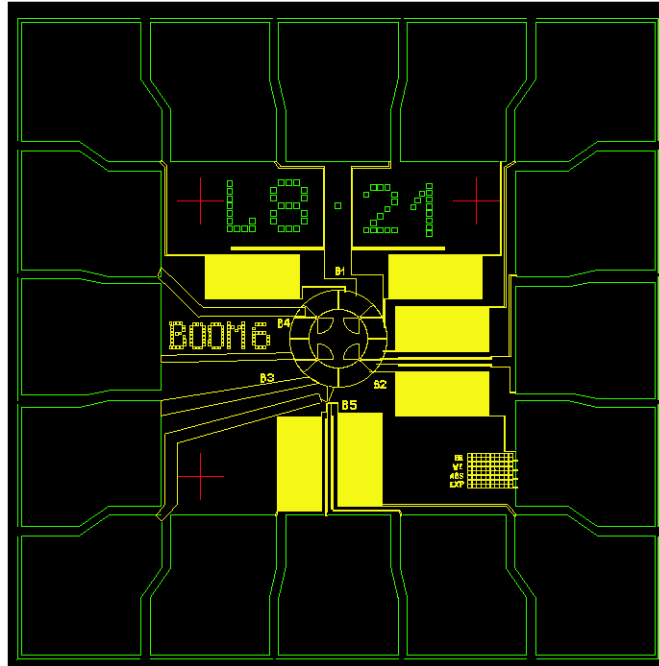


Figure B.1: The CAD layout for the BOOM6 structure.

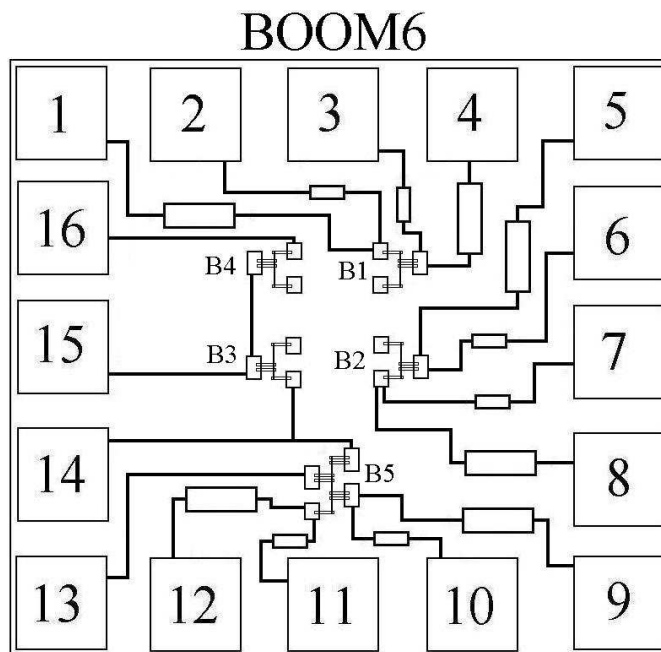


Figure B.2: The simplified layout for the BOOM6 structure.

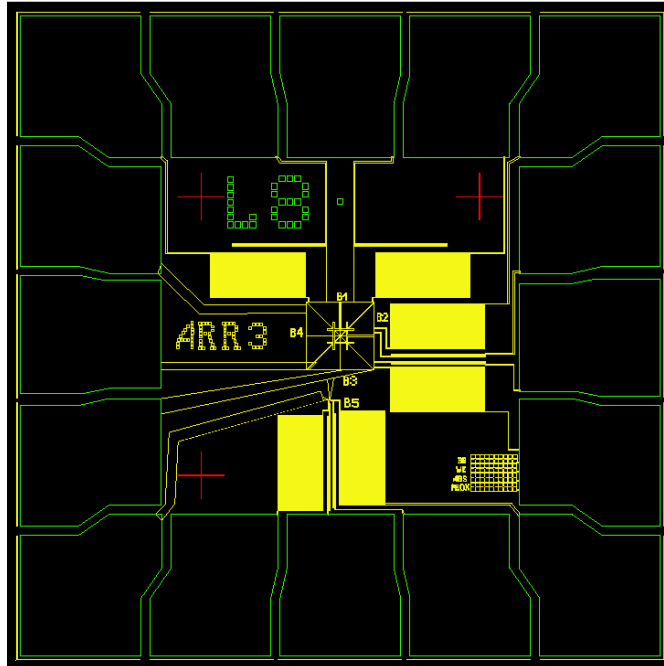


Figure B.3: The CAD layout for the ARR3 structure.

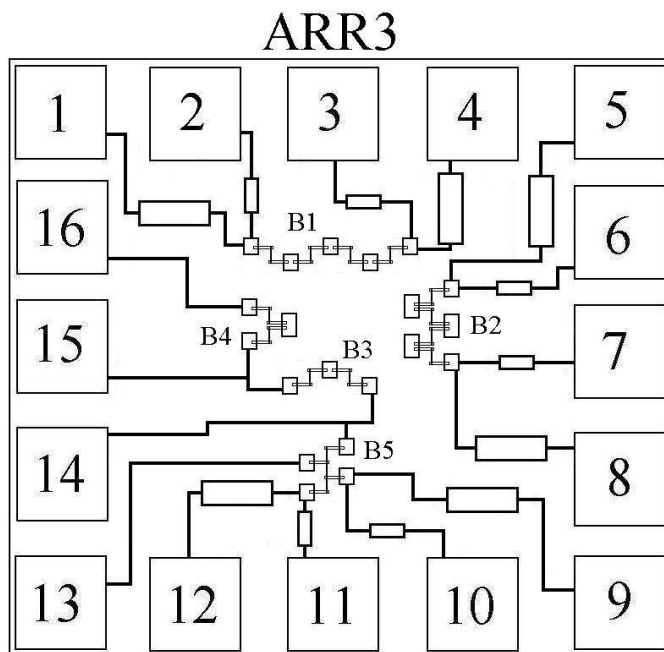


Figure B.4: The simplified layout for the ARR3 structure.

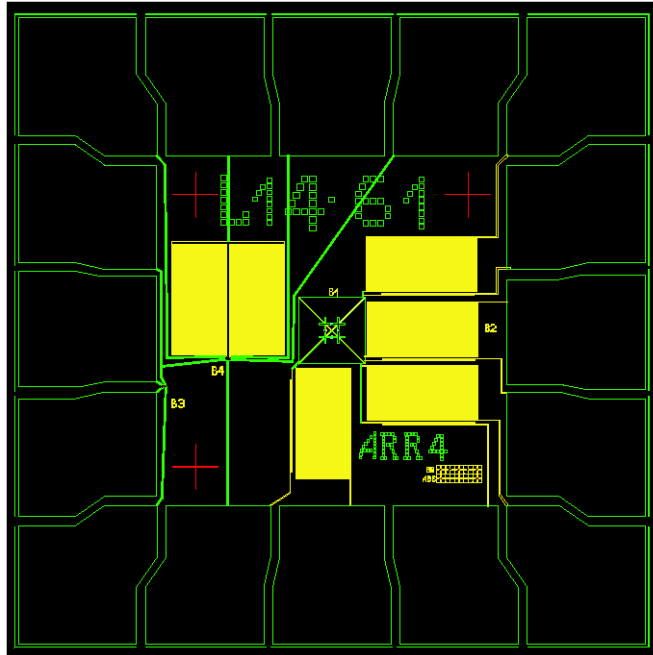


Figure B.5: The CAD layout for the ARR4 structure.

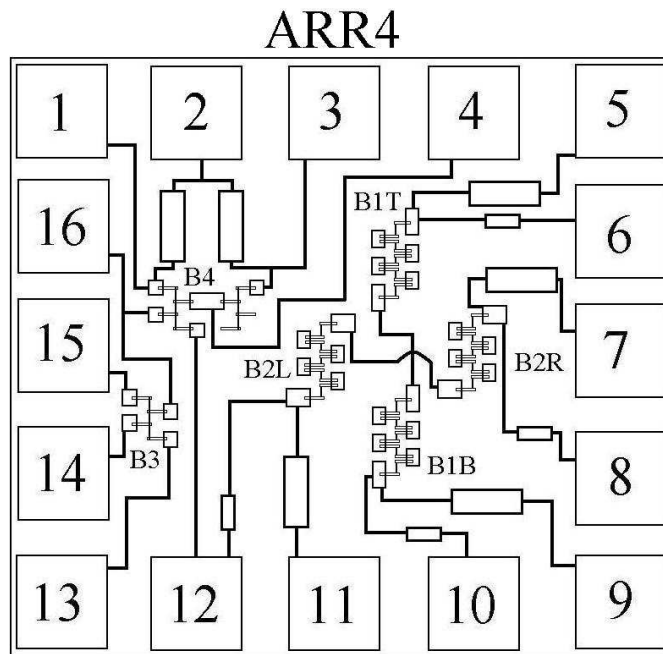


Figure B.6: The simplified layout for the ARR4 structure.

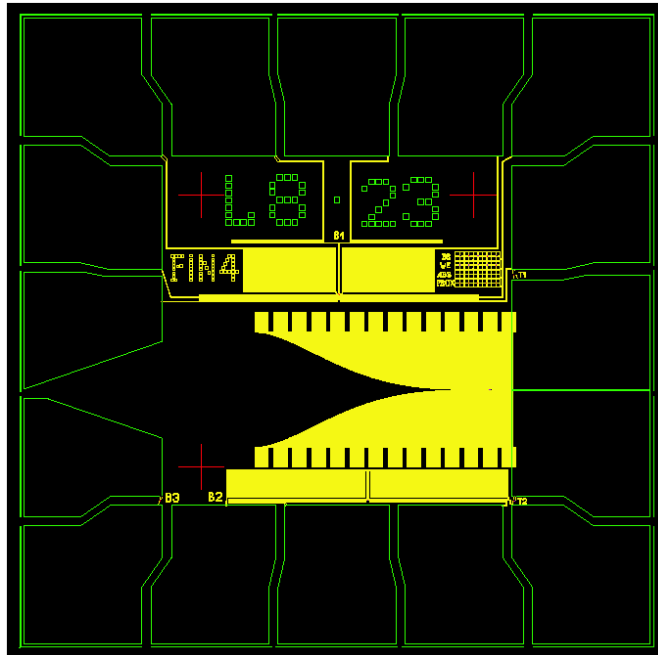


Figure B.7: The CAD layout for the FIN4 structure.

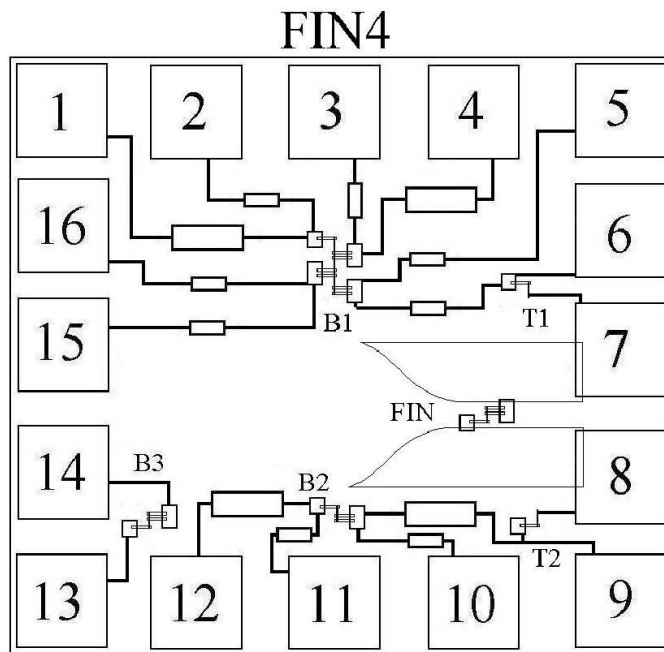


Figure B.8: The simplified layout for the FIN4 structure.

Appendix C

Descriptions of some advanced equipment

C.1 AFM - Atomic force microscope

To get an even more detailed look at the tunnel junctions than the SEM can provide we have used an AFM. The advantages of AFM over SEM are that the latter gives a higher resolution (below 1 nm) and magnification (more than 10^6X), provides a 3D picture of the surface and does not require electron bombardment of the sample, thus making it possible to measure on a real sample without causing damage to it. The main disadvantage is that it requires considerably more time than the SEM to take one good picture of a tunnel junction.

The AFM is a development of the scanning tunnelling microscope (STM). As shown in figure C.1, it uses a cantilever with an extremely sharp tip at the end, held close to the surface. Forces between the tip and the sample surface deflect the cantilever. This deflection is measured by detecting a laser pulse reflected from the top side of the cantilever. Using feedback electronics a signal is then sent to piezoelectric materials attached to the cantilever, adjusting its position to keep it at a constant distance from the sample surface. By scanning the sample surface and registering the adjustments of the cantilever a detailed map of the surface can be created. [34]

C.2 The Heliox cryo system

The Heliox setup is shown in figure C.2. When the samples are loaded and the chamber has been evacuated, reaching a pressure of 10^{-5} mbar, the initial cooling is done by a pulse tube cooler (PTC). The PTC compresses and expands a gas, using a heat exchanger at one end of the pulse tube to

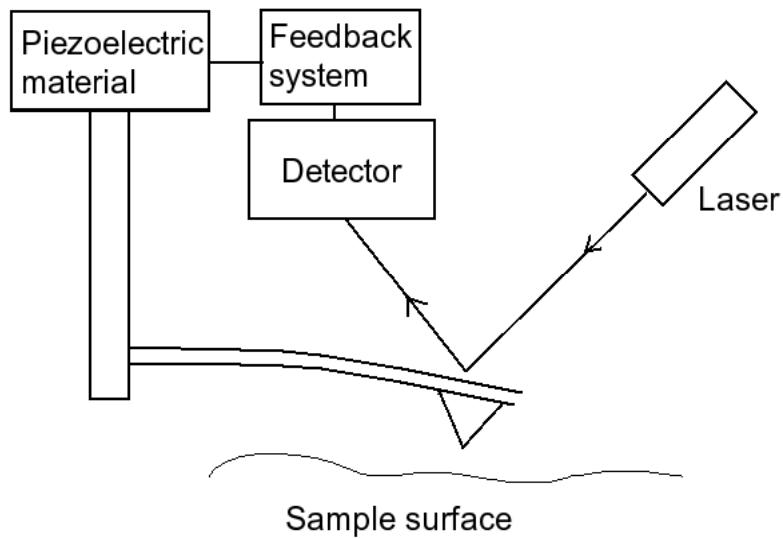


Figure C.1: A sketch showing how an AFM works. The sharp tip of the cantilever is affected by forces from the sample surface, resulting in a deflection of the cantilever which is measured using a laser.

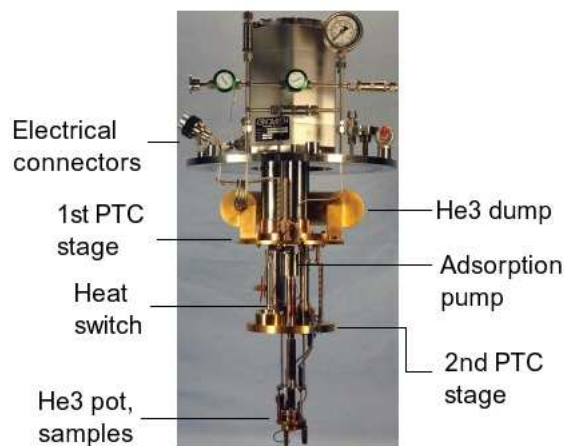


Figure C.2: A picture of the Heliox system with the most important parts marked. [35]

take away heat from the compressed gas and another heat exchanger to let the cooled expanded gas absorb heat from the stage which is to be cooled [36]. This will take the 2nd PTC stage to a temperature just above 3 K. The heat switch connecting the 2nd stage and the adsorption pump (the sorb) is then opened. The sorb heats up to 30 K, causing the ^3He gas which has been pumped there to expand in the chamber. The gas is cooled by the 2nd stage to approximately 3 K before reaching the pot. Gas expansion into the dump causes further cooling and some of the helium at the pot is liquefied. The heat switch is then closed, cooling the sorb causing it to start pumping helium vapour from the pot. This evaporation cooling lets the sample and the pot reach the base temperature (around 300 mK). [23][35]

Appendix D

List of manufactured samples

Table D.1: All our manufactured samples. Samples with the same series no. were produced simultaneously, and hence should show similar characteristics.

Series no.	Name	Type	Absorber structure	Cryo meas.
1	L9-33	BOOM	0.5 nm Cr, 7 nm Al	yes
1	L9-43	ARR3	0.5 nm Cr, 7 nm Al	yes
2	L10-33	BOOM	0.5 nm Cr, 15 nm Al	yes
2	L10-45	ARR3	0.5 nm Cr, 15 nm Al	no
3	L10-55	BOOM	0.5 nm Cr, 10 nm Al	yes
3	L10-63	ARR3	0.5 nm Cr, 10 nm Al	yes
4	L9-31	BOOM	0.3 nm Cr, 19.7 nm Al	no
4	L9-63	ARR3	0.3 nm Cr, 19.7 nm Al	yes
5	L9-35	BOOM	0.2 nm Cr, 19.8 nm Al	no
5	L9-45	ARR3	0.2 nm Cr, 19.8 nm Al	yes
6	L10-32	FIN4	0.2 nm Cr, 10 nm Al	no
6	L10-54	FIN4	0.2 nm Cr, 10 nm Al	yes
7	L10-34	FIN4	0.3 nm Cr, 10 nm Al	yes
7	L10-52	FIN4	0.3 nm Cr, 10 nm Al	no
8	L14-42	ARR4	0.5 nm Cr, 10 nm Al	yes
8	L14-32	ARR4	0.5 nm Cr, 10 nm Al	no
9	L14-21	ARR4	0.5 nm Cr, 7 nm Al	no
9	L14-31	ARR4	0.5 nm Cr, 7 nm Al	no
10	L14-23	ARR4	0.1 nm Cr, 10 nm Al	yes
10	L10-36	FIN4	0.1 nm Cr, 10 nm Al	no

Table D.2: All fabricated samples, with normal and subgap resistance (R_N , R_S), resistance ratio RR , measurement temperature T and type of junctions for each working structure. The bandgap has been divided by the number of junctions in each case. The table is continued on the next page.

Sample/structure	Absorber(nm)	$R_N(\Omega)$	$R_S(\Omega)$	RR	$\Delta(\mu\text{eV})$	$T(\text{mK})$	Type
L1054 FIN4/B1	0.2Cr10Al	0.36k	66k	180		83	SIN
L1054 FIN4/B2	0.2Cr10Al	0.23k	260k	600		60	SIN
L1054 FIN4/B3	0.2Cr10Al	1.2k	78k	66		60	SIN
L1054 FIN4/T1	0.2Cr10Al	0.85k	180k	210		83	SIN
L1054 FIN4/T2	0.2Cr10Al	1.3k	8.6k	7		83	SIN
L1054 FIN4/FIN	0.2Cr10Al	2.4k	120k	48		83	SIN
L945 ARR3/B1	0.2Cr19.8Al	5.1k	120k	23		278	SIN
L945 ARR3/B2	0.2Cr19.8Al	5.7k	130k	22		278	SIN
L945 ARR3/B3	0.2Cr19.8Al	5.1k	54k	10		278	SIN
L945 ARR3/B4	0.2Cr19.8Al	5.4k	57k	11		278	SIN
L963 ARR3/B1	0.3Cr19.7Al	191k	302k	1.6		277	SIN
L963 ARR3/B2	0.3Cr19.7Al	134k	146k	1.1		277	SIN
L963 ARR3/B3	0.3Cr19.7Al	5.2k	60k	12	100	277	SIN
L963 ARR3/B4	0.3Cr19.7Al	6.3k	60k	10	100	277	SIN
L963 ARR3/B5	0.3Cr19.7Al	1.2k	32k	27	100	277	SIN
L933 BOOM/B1	0.5Cr7Al	1.29k	486k	377	220	81	SIN
L933 BOOM/B2	0.5Cr7Al	1.30k	596k	460	210	81	SIN
L933 BOOM/B3	0.5Cr7Al	2.42k	31.2k	13	290	81	SIN
L933 BOOM/B5	0.5Cr7Al	305	136k	446	160	81	SIN
L943 ARR/B2	0.5Cr7Al	4.5k	182k	41			SIN
L943 ARR/B4	0.5Cr7Al	5.8k	82k	14			SIN
L943 ARR/B5	0.5Cr7Al	0.47k	25.7k	46			SIN
L1055 BOOM/B1	0.5Cr10Al	1.35k	1.83M	1357			SIN
L1055 BOOM/B2	0.5Cr10Al	1.8k	642.5k	361			SIN
L1055 BOOM/B5	0.5Cr10Al	0.96k	372.6	387			SIN
L1063 ARR/B1	0.5Cr10Al	3.9k	6.8M	1747		70	SIN
L1063 ARR/B2	0.5Cr10Al	5.0k	3.1M	624		100	SIN
L1063 ARR/B3	0.5Cr10Al	4.6k	170k	37		100	SIN
L1063 ARR/B4	0.5Cr10Al	4.7k	502k	106		100	SIN

Sample/structure	Absorber(nm)	$R_N(\Omega)$	$R_s(\Omega)$	RR	$\Delta(\mu\text{eV})$	$T(\text{mK})$	Type
L1063 ARR/B5	0.5Cr10Al	1.8k	330k	190		100	SIN
L1033 BOOM/B3	0.5Cr15Al	2.1k	32k	15			SIN
L1033 BOOM/B4	0.5Cr15Al	3.3k	44k	13			SIN
L1033 BOOM/B5	0.5Cr15Al	0.29k	25k	87			SIN
L1034 FIN4/FIN	0.3Cr10Al	16k	183k	11		50	SIN
L1034 FIN4/B1	0.3Cr10Al	0.38k	178k	470		80	SIN
L1034 FIN4/B2	0.3Cr10Al	0.2k	227k	1100		80	SIN
L1034 FIN4/B3	0.3Cr10Al	1.2k	261k	219	230	83	SIN
L1034 FIN4/T1	0.3Cr10Al	0.9k	142k	167		80	SIN
L1034 FIN4/T2	0.3Cr10Al	9k	405k	45	260	80	SIN
L1442 ARR4/B4	0.5Cr10Al						SIS
L1032 FIN4/B1	0.2Cr10Al	353	1.89k	5.3		305	SIN
L1423 ARR4	0.1Cr10Al						SIS'